



Investigations of the Moon Phobos by Mars Express and Implications Towards Its Origin

Martin Pätzold¹ · Tom P. Andert² · Alejandro Cardesín-Moinelo³ · Andrea Cicchetti⁴ · Thomas Duxbury⁵ · Yoshifumi Futaana⁶ · James Godfrey⁷ · Sebastian Hegler⁸ · Xuanyu Hu⁹ · Valéry Lainey¹⁰ · Klaus-Dieter Matz¹¹ · Jürgen Oberst⁹ · Roberto Orosei¹² · Dirk Plettemeier⁸ · Pascal Rosenblatt¹³ · Alexander Stark¹¹ · Konrad Willner¹¹ · Olivier Witasse¹⁴ · Ramona Ziese^{9,11}

Received: 7 November 2023 / Accepted: 27 March 2025
© The Author(s) 2025

Abstract

Mars Express has opened a new chapter in the exploration of Phobos, thanks to its elliptical orbit that allows for regular flybys, sometimes as close as 50 km. Initially designed for studying Mars' surface and atmosphere, its instruments have provided a wealth of data, including precise geophysical bulk parameters, insights into Phobos' interior, high-resolution images, remote sensing data of its surface, and observations of interactions between Phobos and the space environment. This resurgence of interest in the Martian moons revolves around the fundamental question of how they formed. Despite the abundance of data gathered by Mars Express, Phobos' surface composition remains uncertain with many unresolved questions. This ambiguity prevents a definitive confirmation or refutation of the asteroid capture scenario, which likens Phobos to a D-type asteroid. This scenario contradicts the current orbits of the moons and poses other dynamical challenges. However, an alternative hypothesis suggests that Phobos and Deimos formed through the accretion of a rocky debris disk in Mars' orbit. Their refined shapes, low mass, and bulk density support this idea. The non-detection of MARSIS echoes implies a porous interior, aligning with the low bulk density, indicative of high porosity. The next phase of Phobos exploration will be led by JAXA's Mars Moon eXplorer (MMX) mission, set to quasi-orbit Phobos, land on its surface, and return a sample to Earth in 2029.

Keywords Mars Express · Mars · Phobos

1 Introduction

The study of Mars' enigmatic moons, Phobos and Deimos, has been a captivating journey of discovery and intrigue, spanning over a century and marked by a series of remarkable investigations. These two moons are named after the sons of the Greek god of war, Ares, who was known to the Romans as Mars – Phobos, meaning “Fear,” and Deimos, meaning “Terror.”

The moons of Mars were discovered by Asaph Hall in August 1877 (Hall 1877). Phobos, a small, irregularly shaped moon just over 22 kilometers mean diameter, is the larger of

Extended author information available on the last page of the article

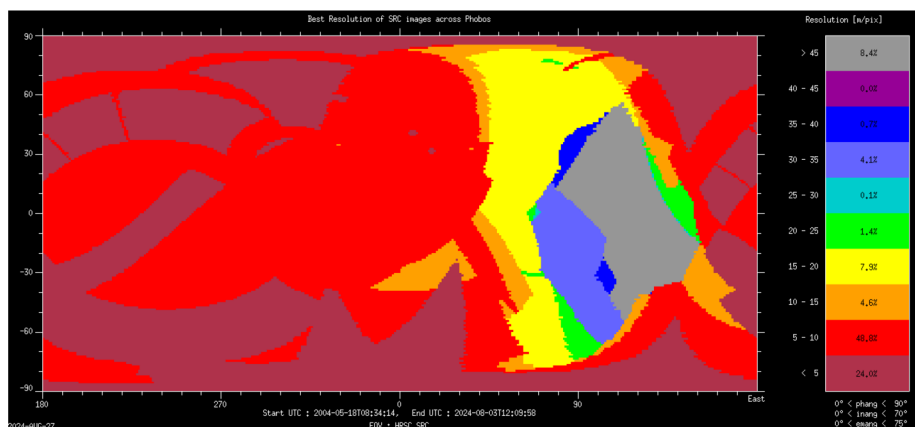


Fig. 1 Resolution of SRC image data at Phobos surface for all SRC observations

Mars' two moons and quickly became the center of scientific curiosity. Early observations from Earth revealed the moon's rapid orbit, completing a full orbit about Mars in a mere 7 hours and 39 minutes at a semi-major axis of 9376 km. This unusual trait sparked a cascade of questions about Phobos' origin, composition, and its potential role in the Martian system.

The origin of these moons remains a subject of intense debate. Before the Mars Express mission, little was known about Phobos and Deimos. Speculation about their origin had persisted since the Mariner 9 mission in 1972 (Pollack et al. 1972). Mariner 9 successfully captured images of both moons due to its orbits bringing the spacecraft into close proximity, though never closer than 5000 km. These opportunities arose because a global Martian dust storm made it impossible to observe Mars' surface, so time initially allocated for surface observations was instead focused on the moons. Despite the distance limitations, the images provided valuable new information about the moons' orbits, rotation periods, sizes, shapes, and surface features.

The Viking mission in 1976 captured several hundred images of Phobos and Deimos (Duxbury 1991) at closer distances and higher resolutions than Mariner 9, completing surface coverage of Phobos at a resolution of 500 m.

Since December 2003, Mars Express has been orbiting Mars, providing valuable insights into Phobos' gravitational field, geological features, and its significance for Martian history and evolution. The mission's close flybys and orbital observations have yielded critical data, illuminating Phobos' formation, its connection to Mars' planetary history, and its potential for future exploration and scientific discovery. Mars Express' polar and highly elliptical orbit enables numerous close encounters (within 1000 km) every five months, as well as a few extremely close flybys (within 100 km) (Witasse et al. 2014).

The High Resolution Stereo Camera (HRSC) on Mars Express, equipped with the Super Resolution Channel (SRC), has also expanded coverage of both moons. While Phobos' surface is fully captured in high-resolution images (see Fig. 1), only Deimos' Mars-facing hemisphere could be imaged, due to its greater orbital distance from Mars—approximately 23,000 km.

Table 3 lists the Mars Express instruments that observed Phobos. Detailed descriptions of these instruments can be found in this special issue.

While Mars Express has provided significant constraints for models explaining the origin of the Martian moons, the full picture remains elusive. Competing theories include asteroid

capture by Mars, simultaneous formation with Mars (Burns 1992), formation in orbit from a debris disk (Craddock 2011), and formation from material ejected into orbit by a large impact on the Martian surface (Rosenblatt et al. 2016).

This paper presents the Mars Express observations of Phobos, focusing on the planning and execution of close and very close flybys, the determination of Phobos' ephemeris, its three-dimensional shape, rotation, geophysical properties, mass, gravity field, and bulk density. It also explores implications for Phobos' internal structure, composition, and origin.

2 Planning of Observations

2.1 Mars Express and Phobos Trajectories

Mars Express follows a highly elliptical and nearly polar orbit around Mars, with an inclination of 86.9° . This orbit is optimized to a low periapsis height between 250 km and 400 km, to achieve the best resolution Mars surface images from the High Resolution Stereo Camera (HRSC) (Jaumann et al. 2007). As a result, the spacecraft's apoapsis reaches up to 11,000 km distance to Mars while Phobos orbits at a distance of approx. 9375 km to Mars (see below for further details).

The orbit of Mars Express gradually changes influenced by the polar flattening of Mars. As a result the longitude of the spacecraft's ascending node shifts westward, opposite to the motion of Phobos. Additionally, it exhibits a slow precession of its pericentre latitude and illumination conditions. Cardesín-Moinelo et al. (2021, Fig. 1) illustrates the evolution of the pericentre precession in latitude, with a period of roughly 20 months or 600 days. This gradual orbital precession leads to the spacecraft's orbit intersecting that of Phobos every 130 or 165 days, called a "Phobos fly-by season", refer to Cardesín-Moinelo et al. (2024, Fig. 5, this collection).

Phobos' orbit is nearly circular with an eccentricity of 0.0151, a periapsis of 9234 km, and an apoapsis of 9517 km. Furthermore, Phobos' orbit is nearly equatorial with an inclination of 1.0756° . Interestingly, the orbital periods of MEX and Phobos are similar. Phobos has a revolution period of 7 hours and 39 minutes, while the orbit duration of Mars Express has varied throughout the mission, ranging from 7 to 7.5 hours. Small variations in this duration have allowed to establish resonances between the two orbits, increasing the number of Phobos fly-bys during their intersections. Several resonances have been applied throughout the mission's lifetime, as detailed in Cardesín-Moinelo et al. (2024, this collection), and since 2018, the mission has been in a stable 23/21 resonance, corresponding to 23 revolutions of MEX and 21 revolutions of Phobos. Due to limited fuel reserves, there are currently no plans to change this resonance for the remaining mission lifetime (expected at least in 2028 or even further).

As the orbits of MEX and Phobos intersect, the minimum distance between them decreases until the crossing, after which it begins to increase again (Fig. 2). The difference in distance between two consecutive fly-bys after 23 MEX revolutions is approximately 437 km. This results in 2 or 3 encounters below 500 km during each Phobos season. The phase angle, which represents the angle between MEX and the Sun as seen from Phobos and is also shown in Fig. 2, indicates that dark/night-side encounters (phase angle >90 deg) occur during the first fly-bys of each season when MEX's orbit is approaching. Bright/day-side fly-bys occur after the closest approach when the distance between the two orbits is increasing. This is due to the orbital configuration of Mars Express and the long-term precession of the line-of-apsides.

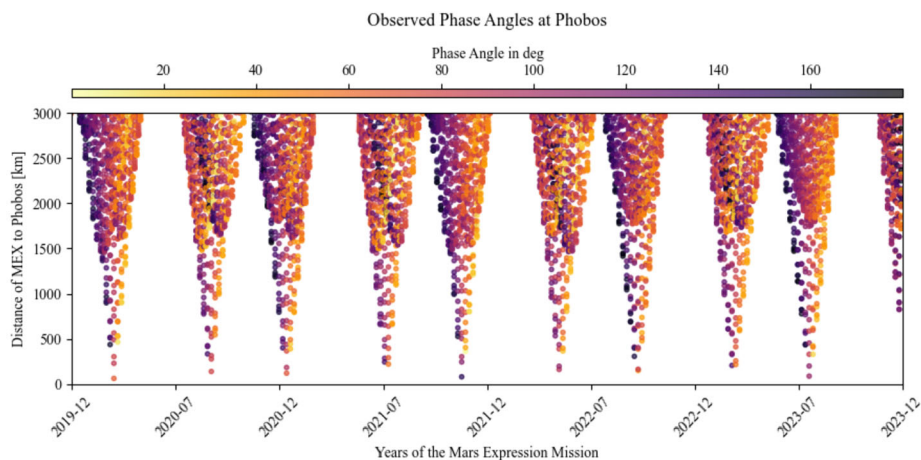


Fig. 2 Mars Express distance to Phobos centre over time. Colour represents the phase angle, that is the angle between the directions toward MEX and the Sun as seen from Phobos at sub-spacecraft point

To optimize close approaches to Phobos, slight adjustments are made to the phase of the spacecraft, aligning both Phobos and the spacecraft near the point of closest approach of their orbits at the same time. These adjustments to the orbital period of the spacecraft are made well in advance to obtain close encounters with minimal fuel consumption. However, the distance is limited for safety reasons. Any orbits passing within 50 km of the Phobos center require the spacecraft to have at least a 1000 seconds phase difference with Phobos to guard against a potential safe mode contingency that could lead to a collision course with Phobos. The 1000 seconds limit is the worst case phase change caused by a disturbance of a double safe mode occurring less than one week before the close encounter, leaving insufficient margin for recovery and collision avoidance maneuvers. The 50 km limit is the worst case cross-track error induced by a disturbance in delta-v, which applies every season to the 5 Mars Express revolutions closest to Phobos' orbit.

2.2 Mars Express Pointing Capabilities to Observe Phobos

Mars Express boasts highly versatile pointing capabilities that facilitate a wide range of observation options during fly-bys. Beyond the standard Mars nadir and limb pointings employed for routine surface and atmospheric observations, the spacecraft can be inertially directed almost anywhere in space (excluding regions near the Sun to prevent illumination issues). This fixed inertial attitude has served as the primary pointing method for most fly-bys throughout the mission, aligning the cameras and spectrometers with Phobos' inertial coordinates at the time of closest approach.

However, inertial pointing approach has its limitations. Particularly, during the closest fly-bys (within 500 km), the high tangential velocity resulted in image smearing effects, and the spectrometer sampling rates were often too rapid, as Phobos remained in the Field Of View (FOV) for only a few seconds. Moreover, even minor phasing errors in Mars Express' predicted trajectory could significantly alter the fly-by geometry, potentially causing a complete miss. On occasions, particularly during very close and fast fly-bys, late pointing and commanding iterations were necessary to compensate for these trajectory phasing errors. To mitigate these issues, various optimizations were applied to the baseline inertial pointing, initially through manual adjustments and later through automated processes.

In 2017, a dedicated Object Tracking pointing mode was developed to autonomously track Phobos for extended durations, allowing for the moon to remain in the FOV for minutes rather than seconds. This improvement resulted in a higher number of acquisitions for the spectrometers and enabled the execution of extended phase curves under varying illumination conditions. Additionally, the tracking pointing method facilitated automatic inertialization, ensuring that the spacecraft's attitude remained fixed concerning the closest approach at any given time. This correction compensated for any potential errors in trajectory predictions and ensured that instrument boresights consistently pointed toward Phobos when necessary, while the camera slit remained perpendicular to the relative movement. This alignment was vital for producing push-broom images with both HRSC and OMEGA. Furthermore, to optimize image quality and avoid smearing effects, derived rotations could be applied at any time, particularly during close fly-bys.

With these versatile pointing capabilities, Mars Express has been able to observe Phobos throughout its orbit in various geometric configurations, at different distances, and under different illumination conditions. This encompassed special events such as transits, occultations, and mutual observations with Mars, the Sun, or other celestial objects. The observations also included monitoring Phobos' shadow on the Martian surface and other diverse geometric scenarios (Oberst et al. 2006a, Witasse et al. 2014, Gwinner et al. 2016, and subsequent sections). These observations not only furnished valuable insights for Phobos science but also endowed additional technical capabilities, including the use of Phobos as a timing reference for instrument calibration purposes, as elaborated in Hernandez-Bernal et al. (2024). Additionally, dedicated pointing methods were developed for specific observations, such as radar reflections on the surface (Cicchetti et al. 2017), radio science measurements of the gravity field (Pätzold et al. 2014b), and plasma monitoring of reflected solar wind protons (Futaana et al. 2021), as discussed in upcoming sections.

2.3 Planning of Phobos Fly-Bys and Other Mutual Event Observations

Over the years, the Mars Express instruments have meticulously planned and performed a substantial number of close-range, as well as more distant astrometric and mutual event measurements, initially summarized in Witasse et al. (2014). This is elaborated in the following sections.

The first observations of Phobos with the HRSC did not take place until orbit 413, on the 18th of May 2004, with a flyby distance of approximately 1900 km. Shortly thereafter, during orbit 756 (cf. Fig. 3), the mission achieved its first close flyby at a distance of about 150 km (Giese et al. 2005). Initially, these observations were planned manually, without the support of dedicated planning software. Later in the mission, an automated planning system was implemented, initially intended for close MEX-Phobos flybys. Planning the imaging for these close encounters proved challenging, as it necessitated a delicate balance of exposure time, slew rate, and pointing precision to capture clear images without smearing or blurring effects. These factors were also contingent on varying illumination conditions and the distance to Phobos. The strategy for astrometric observations of Phobos and Deimos evolved over the course of the mission. Initially, an inertial pointing approach was adopted to ensure that the moons traversed the camera's field of view. However, as the mission progressed, the planning process became more objective-driven. The emphasis shifted towards identifying stars that could be simultaneously captured within the image frame or searching for specific phase angle constellations to facilitate photometric studies.

It was later realized that observations of Phobos and Deimos at greater distances or simultaneous observations of one of these moons with other solar system bodies, such as

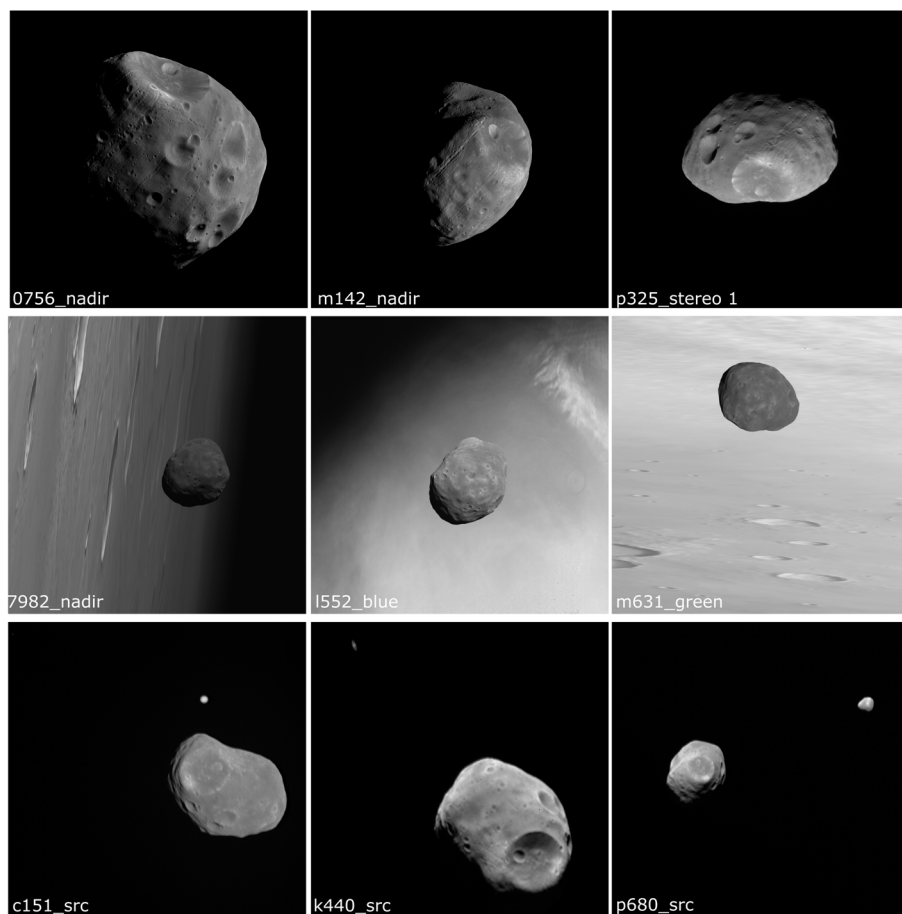


Fig. 3 Phobos as observed by HRSC (first two rows) and SRC (last row). Indicated numbers show the orbit in which the image was acquired and which channel was used to obtain the image. The first row shows images with resolutions of 6 m/pixel, 8 m/pixel, and 55 m/pixel (from left to right). In the second row Phobos was observed above Mars. The last row shows examples of mutual event observations with the SRC - left: Phobos with Jupiter, middle: Phobos and Saturn, right: Phobos and Deimos

Jupiter or Saturn, were of considerable value for obtaining precise astrometric data. These observations, referred to as mutual event observations, could be performed more frequently than direct observations during flybys. This was because a wider range of orbital positions could be utilized, depending on the observational geometry. Moreover, during these events, a sequence of several tens of images could be acquired if necessary, as the relative speeds between the camera and the objects were much lower compared to close flyby observations. The positional measurements derived from mutual event images were independent of the spacecraft's pointing (Ziese and Willner 2018). The abundance of mutual event images, combined with their independence from spacecraft pointing, made this type of observation particularly valuable for orbit modeling algorithms.

Efforts were also made in the past to conduct radar measurements of the surface and sub-surface, utilizing various instrument configurations and yielding promising results (Cicchetti

et al. 2017). However, the instrument was not originally designed for Phobos observations, and its capabilities were significantly constrained. Since 2023, the MARSIS instrument's on-board software has undergone upgrades, enhancing its flexibility and potential for Phobos observation. This new on-board software incorporates several improvements aimed at enhancing signal reception and on-board data processing, ultimately increasing the quantity and quality of science data transmitted to Earth. This upgraded software is now operational and has significantly expanded the observation capabilities, offering an unprecedented level of detail in Phobos observations, as indicated by its preliminary results (Cicchetti et al. 2023). Last, it has been shown recently that MARSIS measurements can now be used for constraining Phobos' orbit (Desage et al. 2024).

3 Phobos Ephemerides

3.1 Ephemerides from MEX Radio Tracking

Mars Express significantly contributes to the precision of Phobos ephemerides, primarily through astrometric observations made using the Super Resolution Channel (SRC) as part of HRSC. These observations have undergone meticulous processing, relying on the navigation orbit provided by the European Space Operations Centre (ESOC). However, it is important to note that the navigation orbit carries a certain level of error, directly impacting the accuracy of Phobos ephemerides by introducing a positional bias.

In an effort to improve this situation, Rosenblatt et al. (2008) computed a more precise orbit for the spacecraft. This refined orbit was employed to reduce a subset of SRC observations, marking a departure from the conventional reliance on the navigation orbit. This approach yielded a notable improvement, enhancing the accuracy of Phobos ephemerides by approximately 25 meters. Nevertheless, it is worth noting that this enhancement, while significant, still falls short of fully compensating for the error attributed to the intrinsic orientation of the SRC camera.

Additionally, the availability of this highly accurate orbit for Mars Express opened up an opportunity to refine the solution for Phobos' mass (Rosenblatt et al. 2008), a pursuit with roots dating back to the Viking era. This new mass solution underwent further refinement through dedicated close flybys, aimed at precisely determining Phobos' gravity field, as detailed in Andert et al. (2010) and Pätzold et al. (2014b).

The ephemerides of Phobos and Deimos are determined by fitting a model of their orbital motion to astrometric observations. The first models were developed nearly a century ago based on analytical theories of the moons' orbits (see Jacobson and Lainey 2014). These early models allowed for the estimation of the mean motions of the moons along their orbits and the precession rates of this motion in the orbital plane. As time progressed, these models were improved by introducing expected secular accelerations to the mean motion, which led to the first estimation of Phobos' orbit decay (Sharpless 1945). These models continued to evolve, and they were used until the space age to predict the positions of Phobos and Deimos.

However, these predictions proved insufficiently precise for the Viking spacecraft's operations during multiple flybys of Phobos, which aimed to determine the mass of Phobos (see Jacobson and Lainey 2014). To address this, numerical models were developed specifically for the Viking flybys (Tolson et al. 1977). Subsequently, Lainey et al. (2007) developed the first complete numerical model, incorporating the effect of Mars' gravity field harmonics, perturbations from the Sun and other planets, gravitational interactions between both

moons, tidal effects raised on Mars by both moons (responsible for Phobos' orbital decay), and the effect of Phobos' shape on the moons' orbits. These authors used a compilation of astrometric data until the first SRC observations by Mars Express to fit their numerical model. Jacobson (2010) extended this numerical model by incorporating the effect of Phobos' libration, providing an independent estimate of Phobos' rotation parameters, which complements the estimations performed using SRC images of Phobos' surface (see Oberst et al. 2014). The latest libration values from the ephemerides suggest a slightly heterogeneous mass distribution inside Phobos (Jacobson and Lainey 2014; Lainey et al. 2021). The fit of the numerical model to astrometric observations also yields an estimation of the tidal dissipation rate inside Mars, as inferred from the Phobos orbital decay. This rate is subsequently used to constrain Mars' interior structure and evolution (Samuel et al. 2019).

In preparation for the very close flyby of Phobos in 2013, SRC images were taken both before and after the event, resulting in an accurate ephemeris of Phobos, with an error in the range of a few hundred meters at the time of the flyby (Lainey et al. 2021). This refined ephemeris significantly aided in determining the gravity field of Phobos through the Doppler tracking of Mars Express during the close flyby (Pätzold et al. 2014b). The latest ephemerides of Phobos and Deimos are estimated to have a formal error of approximately 400 meters (1σ) at the time of the MMX mission (between 2025 and 2030) (Lainey et al. 2021).

3.2 Ephemerides from SRC Astrometric Observations

The first close encounters of Phobos by Mars Express, with a particular focus on the observations made by the Super Resolution Channel (Oberst et al. 2008) of the HRSC, unveiled significant discrepancies between the predicted positions of the Martian moon and the actual positions observed in the images. These predicted positions were calculated by the navigation teams at the Jet Propulsion Laboratory (JPL) in Pasadena, California, and the European Space Operations Center (ESOC) in Darmstadt, Germany. The discrepancy became evident during the initial attempts to capture images of Phobos with the SRC, as the camera was pointed in the wrong direction, and Phobos never entered the field of view of the SRC.

Oberst et al. (2006b) presented a series of astrometric observations based on SRC frame images. The authors fitted a triaxial ellipsoid model to the observed limb of Phobos, demonstrating that the predictions of Phobos' positions by JPL and ESOC at that time had an offset of several kilometers from the moon's actual position. Consequently, the astrometric observations obtained by the SRC for both Phobos and Deimos were utilized to update the ephemerides of these moons (Lainey et al. 2007, 2021; Jacobson 2010).

Over time, techniques for image reduction evolved with changing observation strategies and an improved understanding of Phobos' bulk properties. While the limb fitting techniques used by Oberst et al. (2006b) still required visibility of large portions of the limb, the control network fit method used by Willner et al. (2008) only needed a small fraction of the moon to be visible, as the center of figure location was inferred from control point positions on the surface of Phobos. However, the accuracy of this method still depended on the precision of the control points and the camera pointing accuracy to derive absolute values for right ascension (RA) and declination (DEC).

Pasewaldt et al. (2012, 2015) once again employed the limb fitting method for either of the Martian moons but, instead of the limb of an ellipsoidal body, they used the limb of their shape models (Willner et al. 2010a, 2014) to obtain a more accurate limb outline. This allowed the center-of-figure (COF) to be inferred from the shape model. For this approach, it was advantageous if large parts of the limb were visible. Additionally, Pasewaldt et al.

(2015) determined astrometric positions of Phobos by using the control point network information from Willner et al. (2010a) and compared those with astrometric positions derived by the limb fitting routine. It turned out that the limb-fitting method was, in most cases, less favorable in direct comparison with the observations of the control point network.

Oberst et al. (2006b), Willner et al. (2008), and Pasewaldt et al. (2012, 2015) controlled the pointing of the spacecraft by evaluating images of stars obtained in the first and last images of the close flyby series, i.e., just before and after the encounter with the moon. This provided only limited control, as the spacecraft was often not fully stable after being oriented towards the moons and continued to sway during a series of images. Thus, even for subsequent images, the pointing could differ significantly.

Ziese and Willner (2018) evaluated mutual event images of the moons, where Phobos and Deimos or one of the moons and either Jupiter or Saturn were visible. Instead of measuring the positions of the moon, they determined the angular separation between the planetary objects. Unlike the single positions of the objects, their angular separation was independent of the spacecraft's pointing and, therefore, more accurate. Additionally, for images with Jupiter or Saturn in the background, they provided RA and DEC of the moon in the foreground. To achieve this, they used the predicted RA and DEC of Jupiter/Saturn and the change in RA/DEC of the moons with respect to Jupiter/Saturn (again, independent of the spacecraft's pointing) to compute RA and DEC of the moon. The COFs of the moons were determined by creating a simulated version of the measured image using the predicted positions of the moons, their shape (Willner et al. 2014; Thomas et al. 2000), and rotational models (Stark et al. 2017; Archinal et al. 2018). The center-of-mass (COM) of Phobos or Deimos was known in the respective simulated image by reconstruction. Assuming that the COM and the COF coincided, the COF of the moon in the measured image was then determined by matching the simulated moon with the moon in the measured image.

All the astrometric observations were continuously used to maintain the accuracy of the orbital models for the Martian moons and further enhance our knowledge about bulk properties, such as rotational parameters (Lainey et al. 2021; Jacobson and Lainey 2014).

4 Geodesy and Geophysical Bulk Parameters

4.1 Shape Models

The High-Resolution Stereo Camera (HRSC) stands out as a unique tool in planetary exploration, with its built-in stereo capability and additional color channels (Jaumann et al. 2007). This distinctive combination empowers photogrammetric analysis from a single planetary body flyby. Its efficacy was prominently demonstrated during orbit 0756 when HRSC captured stereo images of Phobos with 10 to 20 m/pixel resolutions in full color, pioneering the creation of a first regional HRSC digital terrain model (Giese et al. 2005) of Phobos. With a grid spacing of 100 to 200 m it was a significant improvement over the previous established shape model based on Viking Orbiter image data (Gaskell 2002), the latter providing a grid spacing of approx. 400 m at the equator derived from image data of approx 200 m/pixel ground resolution. As more data were collected, it led to the development of a global digital terrain model and a spherical harmonic function model (Willner et al. 2010a). These advances hinged on the utilization of photogrammetric stereo techniques. The shape models, following additional stereo image data collected during close HRSC flybys, were further refined by Willner et al. (2014) (cf. Fig. 4).

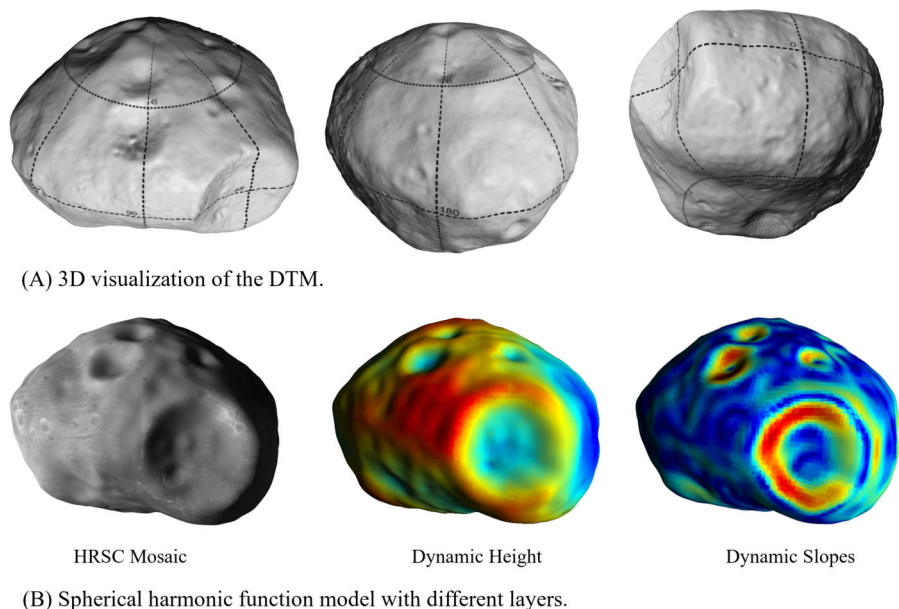


Fig. 4 Shape model displays as in Willner et al. (2014). Display (A) shows rendered images of the digital terrain model while (B) displays the derived spherical harmonic function model with additional layers in a 3D context

These shape models played a pivotal role in refining the volumetric data of Phobos. Together with the mass determined by radio tracking data (Andert et al. 2010; Pätzold et al. 2014b), the moon's mean density was derived (see Sect. 4.3).

4.2 Rotation and Reference Frame

Prior to the Mars Express mission, the Phobos reference frame relied on a control point network derived from Viking Orbiter image data (Duxbury 1974; Duxbury and Callahan 1989), with the certainty of the control point coordinates varying significantly depending on their location. In addition to providing surface coordinates, this analysis allowed for the derivation of information regarding bulk properties, such as the best-fitting ellipsoid parameters and the amplitude of the forced libration in longitude. This libration, a superimposed oscillation on Phobos' mean rotation rate, results from the gravitational torque of Mars acting on Phobos' elongated shape. The amplitude of this libration offers additional insights into Phobos' interior structure, specifically its moments of inertia.

With the Super Resolution Channel of HRSC observing Phobos from close range, and thus providing higher resolution, the number of control points could be increased, significantly improving accuracy (Willner et al. 2010a). This enhancement led to new estimates of the forced libration amplitude, falling within the range of -1.09 deg (Oberst et al. 2014), -1.143 deg (Burmeister et al. 2018), and -1.21 deg (Willner et al. 2010a). Various methods were employed to determine the amplitude, with Willner et al. (2010a) applying an empirical approach, Oberst et al. (2014) analyzing the error distribution, and Burmeister et al. (2018) solving for the amplitude as part of a bundle block adjustment. All three results fell within each other's error margins but significantly diverged from pre-MEX information.

The coordinate frames of the control points were centered at the center of figure (COF) of the derived shapes, with the coordinate axes aligned with the moments of inertia axes.

Apart from the libration amplitude, all other rotational parameters of Phobos were derived from its orbit, assuming that the rotational axis was perpendicular to the orbital plane and that the rotation rate matched the mean orbital motion (Stark et al. 2017; Jacobson et al. 2018). However, the above-mentioned refinements of the ephemerides were not immediately integrated into the rotational model for Phobos and Deimos (Rambaux et al. 2012). This discrepancy between orbital and rotational dynamics became evident when an offset between Phobos' longest axis and the direction towards the center of Mars during periapsis or apoapsis was observed. A difference between the modeled and observed orientation was also noted in the simulated images used for astrometric observations (Ziese and Willner 2018). Both Stark et al. (2017) and Jacobson et al. (2018) refined the rotational models for the Martian satellites based on the available ephemerides models. Archinal et al. (2018) came to the conclusion to recommend the use of Stark et al. (2017) rotational model for Phobos and Deimos. This model, along with the current ephemerides models, owes much to the almost two decades of observational records collected by Mars Express (Lainey et al. 2021).

4.3 Phobos Mass, Gravity Field and Bulk Density

Several methods have been employed in the past to determine the mass of both Phobos and Deimos, including:

- (a) Close flybys by spacecraft, where the immediate perturbed Doppler shift of the transmitted radio signal is analyzed.
- (b) Distant encounters, which involve the analysis of the long-term perturbations of the spacecraft's orbit.
- (c) global gravity field solutions.

These methods have collectively advanced our understanding of the masses of Phobos and Deimos. For a comprehensive review of all techniques, mass estimates, and comparisons, refer to Pätzold et al. (2014a). This section primarily focuses on mass determinations obtained from close flybys of Mars Express, conducted as part of the Mars Express Radio Science (MaRS) experiment. Spacecraft radio tracking is generally considered the most accurate method for such measurements.

When a spacecraft approaches a planetary body at a sufficiently close range, the body's gravitational force influences the spacecraft, causing perturbations in its velocity and trajectory. These changes in velocity are measured by detecting perturbations in the Doppler frequency shift of the spacecraft's transmitted radio signal during the flyby. The observed Doppler shift is directly proportional to the gravitational force, represented by $G \cdot M$, the product of the gravitational constant G and the mass of the body M (Anderson 1971; Pätzold et al. 2001).

The first mass determinations of Phobos were conducted by the Viking mission in 1977, involving 17 encounters within 300 km of the moon, with one approach reaching as close as 89 km. Several mass estimates were derived from the mission's tracking data (Christensen et al. 1977; Tolson et al. 1977; Williams et al. 1988).

In 1989, the Phobos 2 mission was launched and placed in a quasi-satellite orbit around Phobos. During this mission, the spacecraft successfully rendezvoused with Phobos, approaching as close as 500 km during 22 orbits before concluding operations on March 27, 1989. Analysis of the tracking data from these flybys by Kolyuka et al. (1990) yielded a precise mass estimate. However, the specific methodology used for formal error estimation was not disclosed.

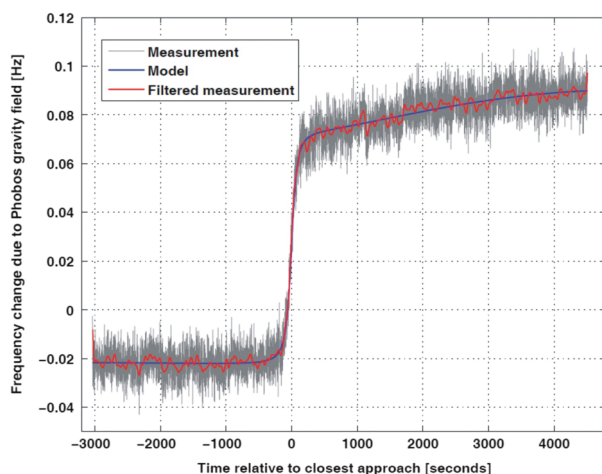


Fig. 5 Change in radio carrier frequency (or Doppler velocity) residuals (observed frequency minus predicted frequency not considering the mass of Phobos as a perturbing force) at X-band (8.4 GHz) as a function of time relative to the closest approach (275 km) of Mars Express to Phobos on July 17th 2008. The rapid change of the frequency residuals (grey) is a measure of the perturbing force (mass). The constant pre-encounter bias is caused by forces not considered by the prediction and will be eliminated by the model fit (blue solid line). The red solid line is filtered at a time step of 18 s. Figure taken from Andert et al. (2010)

Table 1 Solutions for $G \cdot M$ and the gravity coefficients C_{20} and C_{22} of Phobos have been obtained from various Mars Express flybys. The error bar is set at 1σ

Date	distance (km)	$G \cdot M$ ($10^6 \text{m}^3 \text{s}^{-2}$)	C_{20}	C_{22}
23.03.2006 ^(a)	459	0.7120 ± 0.0120	-	-
17.07.2008 ^(a)	275	0.7127 ± 0.0021	-	-
03.03.2010 ^(b)	77	0.7072 ± 0.0004	-0.1145 ± 0.0485	0.0025 ± 0.0018
03.03.2010 ^(c)	77			
29.12.2013	58	0.70765 ± 0.00025	-0.1378 ± 0.0116	0.0166 ± 0.0051

^(a) Andert et al. (2010); ^(b) Pätzold et al. (2014b); ^(c) Yang et al. (2019).

Mars Express, with its nearly polar orbit, became the next spacecraft capable of executing close flybys of Phobos. The details of the four close MEX flybys performed between 2006 and 2013, which were utilized for mass determination, are presented in Table 1. Phobos behaves as a point mass for flyby distances greater than 70 km, similar to the very first two MEX flybys. As an example, the Doppler shift of the radio carrier caused by the attracting force of Phobos during flyby on July 17th 2008 is shown in Fig. 5. The flyby geometry during this flyby was optimal and the final Doppler shift of about 70 mHz at X-band is a measure of the gravitational mass $G \cdot M$ (Pätzold et al. 2001). At the last two flybys, it became possible to resolve the gravity coefficients of degree and order two, albeit with a relatively high margin of error (Table 1).

The observed gravity coefficients C_{20} and C_{22} in Table 1 are compared with the theoretical coefficients $C_{20,\text{shape}} = -0.106 \pm 0.01$ and $C_{22,\text{shape}} = -0.015 \pm 0.002$, calculated from the shape model (Willner et al. 2010a). These calculations assume a homogeneous internal mass distribution and a constant bulk density (Pätzold et al. 2014b). Any discrep-

ancies between the observed C_{20} and C_{22} values (Table 1) and the theoretical values for a homogeneous Phobos suggest deviations from a uniform internal mass distribution.

The bulk density of a planetary body provides first insights into its composition and internal mass distribution. The mass M of Phobos, as computed from the last $G \cdot M$ entry in Table 1, is (Pätzold et al. 2014b):

$$M = (1.05 \pm 0.02) \times 10^{16} \text{ kg} \quad (1)$$

Together with the volume of Phobos, determined by HRSC (Willner et al. 2014) as

$$V = (5742 \pm 35) \text{ km}^3, \quad (2)$$

the bulk density is then calculated to be

$$\rho = (1860 \pm 13) \text{ kg/m}^3. \quad (3)$$

This value is significantly lower than what would be expected if Phobos were composed solely of solid, rocky material. There are three possibilities: Phobos may be made up of lighter materials mixed with rocky materials, or it may possess a substantial amount of porosity, or both.

The internal structure of bodies as small as Phobos can be categorized into three types:

- Differentiated Structure: Some bodies may exhibit a differentiated interior, characterized by multiple layers with increasing density as one moves towards the center. This layered composition can result from geological processes and the separation of materials over time. However, the size of Phobos and its density may be too small to undergo differentiation. Although partial differentiation is suspected for larger asteroids, such as (21) Lutetia (the flyby object of the Rosetta mission on its way to comet Churyumov-Gerasimenko in 2011), (21) Lutetia is about five times larger, with a density approximately twice that of Phobos (Pätzold et al. 2011; Weiss et al. 2012).

- Homogeneous Composition: Some bodies have a more uniform and homogeneous interior, with constant density throughout. This uniformity can arise from the accumulation of similar materials or a lack of significant geological differentiation.

- Rubble Pile-Like Structure: A rubble pile is a structure where the interior is composed of loosely packed material with clusters of varying densities. Such structures often form when smaller objects accumulate under the influence of gravity, creating regions of differing densities within the body.

Figure 6 from Pätzold et al. (2014b) shows the rock material density as a function of volumetric porosity content $\frac{V_{\text{porosity}}}{V}$ along constant lines of volumetric water ice content $\frac{V_{\text{water}}}{V}$.

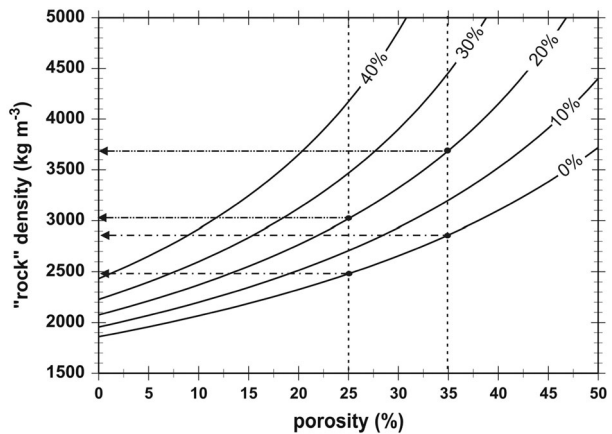
For a non-porous body $\frac{V_{\text{porosity}}}{V} = 0$ and no water ice content $\frac{V_{\text{water}}}{V} = 0$, the solid rock density is, of course, that of the bulk density and much too low.

If the porosity value increases, the rock density must also increase to satisfy the constraint of the observed total mass and bulk density. Rocky material densities between 2500 kg/m^3 to 2900 kg/m^3 require for example porosities between 25%–35%. Higher rocky material densities above 3000 kg/m^3 require porosities beyond 40%. It is a point of discussion whether macro-porosities beyond 40% from accretion of larger debris objects in orbit can be maintained by a body as large as Phobos. However, Phobos would not be able to survive an impact which formed the Stickney crater without a large degree of porosity (Housen et al. 1999).

Table 2 Simulated C_{20} and its 1σ error for various water ice contents and porosities (taken from Pätzold et al. 2014b)

porosity%	water ice %	C_{20}
0	0	-0.1068 ± 0.01
0	20	-0.1134 ± 0.003
30	0	-0.1267 ± 0.008
30	20	-0.1422 ± 0.016

Fig. 6 Rock density as a function of porosity and water ice content taken from Pätzold et al. (2014a). The rock density corresponding to a $30\% \pm 5\%$ porosity (Andert et al. 2010) and a 0% water ice content, for example, is in the range 2500 to 2850 kg/m^3 . For the same porosity range but 20% water ice content, the resulting rock density is 3000 to 3700 kg/m^3



Rosenblatt (2011) also suggests that water ice constitutes a fraction of Phobos' composition. The inclusion of lighter materials, such as water ice, implies that the densities of the rocky material must be significantly higher than 2500 – 2900 kg/m^3 in the example above or that porosities must be lower. The solid lines in Fig. 6 represent lines of constant water ice content. For a Phobos with 25% – 35% porosity and 20% water ice content, the required rock densities range from 3000 – 3700 kg/m^3 .

Pätzold et al. (2014b) simulated the interior of Phobos by dividing its volume into numerous elements, each assigned random properties such as mass (or density) or porosity (representing voids with zero density). For a homogeneous mass distribution with the observed bulk density, zero water content, and zero porosity, the simulation should reproduce the total mass and the $C_{20, \text{shape}}$, which it successfully does (see Table 2).

The simulation further demonstrates that C_{20} increases to larger (negative) values with greater errors (broader distributions) as the water ice content and porosity increase.

When comparing the simulated C_{20} with the observed values reported by Pätzold et al. (2014b) and Yang et al. (2019) based on two combined MEX flybys $C_{20} = -0.1145 \pm 0.1456$ and $C_{20} = -0.1378 \pm 0.0348$, respectively (see Table 2), the results suggest a tendency toward a combination of water and porosity in addition to the rocky elements. However, the large uncertainties in the observed C_{20} measurements prevent a definitive conclusion of the amounts.

5 Surface, Sub-Surface and Space Environment Observations

5.1 Surface Morphology: Crater Statistics, Grooves, and Slopes

Phobos' surface is heavily cratered and characterized by the well-known "Phobos grooves", a series of striations that cover a great deal of the moon's surface (Soter and Harris 1977a; Thomas et al. 1978). HRSC image data now cover more extensive areas on Phobos, revealing finer details, especially on the Phobos farside and the trailing hemisphere. Schmedemann et al. (2014) produced updated crater production and chronology functions for two scenarios: (i) in which Phobos has been in its current orbit around Mars since its formation, and (ii) an alternative scenario where Phobos was captured as an object from the Main Asteroid Belt. The results suggest that Phobos either formed through a significant collision about 4.3 billion years ago or was captured approximately 3.66 billion years ago in the case of capture. The age of the large Stickney crater was estimated to be around 4.18 billion years or 3.54 billion years in the case of capture. However, other studies suggest a much younger age for Stickney assuming that a majority of impact craters are secondary impacts as a result of the impact causing Stickney (Ramsley and Head 2017).

Moreover, the HRSC images allowed for a comprehensive mapping of the distinctive Phobos grooves, offering a more detailed view of the groove population (Murray and Heggie 2014). Researchers identified several distinct "families" of grooves of varying ages. While grooves seem to be a global phenomenon, they appear to be concentrated on Phobos' leading edge. In contrast, areas on the trailing hemisphere completely lack grooves, forming what is referred to as "zones of avoidance." Various explanations have been proposed for the formation of these grooves, including fracturing due to tidal forces (Simioni et al. 2015), representation of chains of secondary impacts (Ramsley and Head 2019), or formation through impacts with Phobos moving through orbiting debris. Murray and Heggie (2014) argue that Phobos' grooves resulted from a series of brief bombardments by ejecta particles from primary impacts on Mars. Based on crater statistics (Schmedemann et al. 2014), it is estimated that grooves may have formed throughout the history of Phobos, as early as 4.04 billion years ago and possibly as late as 0.224 billion years ago.

The presence of landslides on steep slopes on Phobos provides unique insights into the satellite's dynamic orbital evolution. It is well-known, however, that Phobos is gradually approaching its host planet due to tidal interaction and friction. Shi et al. (2016) utilized the new HRSC images and gravity working models (Shi et al. 2012) to map the distinct distribution pattern of mass wasting on steep crater walls. Their findings suggest that landslides may have been triggered by increasing tidal forces and escalating slope angles on these walls.

5.2 Surface Composition

The surface composition of Phobos can be determined through the use of UV, visible, near-IR, and thermal spectrometers. However, when comparing the results from the OMEGA (Fraeman et al. 2012), PFS (Giuranna et al. 2011) and SPICAM (Witasse et al. 2014) spectrometers, these are conflicting and disputed.

The OMEGA (Observatoire pour la Minéralogie, l'Eau, les Glaces et l'Activité) imaging spectrometer investigated the surface composition of Phobos with two channels (Visible 380-1050 nm, and IR 930-5000 nm), revealing the presence of minerals such as pyroxene, olivine, and phyllosilicates. These findings are consistent with a primitive composition for Phobos, in agreement with laboratory spectra from Tagish Lake, a D-type asteroid meteorite analog. This suggests that Phobos may be a captured D-type asteroid. These spectral

properties, however, do not align with the bulk composition and basaltic crust/lithosphere composition of Mars (Fraeman et al. 2012).

In contrast to the OMEGA results, the observations made by the Planetary Fourier Spectrometer (PFS) in the thermal Infrared (1.2–45 μm) do not match the spectral features of any chondritic meteorite analogs or primitive materials. PFS has identified various minerals on Phobos, including pyroxene and olivine, which are common components of rocky asteroids. The PFS findings lean towards the conclusion that Phobos is not a captured asteroid and instead suggest an in-situ formation for Phobos (Giuranna et al. 2011).

The SPICAM instrument (SPECTROSCOPY for the INVESTIGATION of the CHARACTERISTICS of the ATMOSPHERE of MARS) is a two-channel spectrometer (UV 118–320 nm, IR 1.1–1.7 μm) designed for nadir and limb viewing in the UV and IR regions, allowing for the determination of vertical atmospheric profiles during solar and stellar occultations. The UV spectrum observed by SPICAM during Phobos flybys exhibits a dip at 220 nm, which is interpreted as being caused by polycyclic aromatic hydrocarbons (PAH). Another prominent dip at 350 nm suggests the presence of ilmenite, a titanium-iron oxide mineral, as the underlying cause (Bertaux et al. 2011). Ilmenite has also been found in moon rocks.

5.3 Subsurface Sounding

An unexpected development in the utilization of the subsurface sounding radar MARSIS, short for “Mars Advanced Radar for Subsurface and Ionospheric Sounding”, was its successful sounding of Phobos, despite the challenges posed by its small size and curved surface, which make it a radar target with weak backscattering properties. MARSIS operates at a frequency range of 1.3 - 5.5 MHz and is designed to probe the surface and subsurface of Mars to depths ranging from a few hundred meters to 3.7 km beneath its southern polar layer deposit (Picardi et al. 2005). Originally, MARSIS was designed exclusively for observing Mars, but the high eccentricity of the Mars Express orbit allowed for observations of the Martian moon Phobos during several close flybys. For safety reasons, software and hardware protection mechanisms prevent MARSIS operation when the target is closer than 240 km. To enable operation at distances closer than this, the radar had to be reconfigured to bypass protections partially while maintaining a high level of safety, including preventing the opening of the receiver until a certain time elapsed after transmission. Furthermore, normal on-board processing was insufficient due to the relatively large uncertainties in spacecraft velocity and time of closest approach during flybys. Therefore, it was necessary to store raw echoes in the instrument’s mass memory and transmit them to the ground at a later time. Recently, a new on-board software (SW) was designed to optimize the observation of Phobos, enabling the observation of this remarkable target even at distances below 50 km. Although the new on-board SW is still undergoing testing, the latest observations of Phobos have shown very promising results.

The first opportunity for MARSIS to observe Phobos occurred on November 4th, 2005, when MARSIS approached within 215 km of its surface during Mars Express’ orbit number 2323. During this flyby, MARSIS collected data over a period of approximately 5 minutes, ranging from a distance of 460 km to 215 km, and then extending out to 430 km. Approximately 16,000 raw echoes were collected and stored in the instrument’s on-board memory. Despite Phobos’ relatively small size and the challenges associated with low antenna gain due to the radar’s large wavelength, the observed signal-to-noise ratio (SNR) reached approximately 25 dB. Subsequent flybys brought MARSIS even closer to the surface, but the radar’s design limited its operations to a minimum target distance of 172 km (Safaenili et al. 2007).

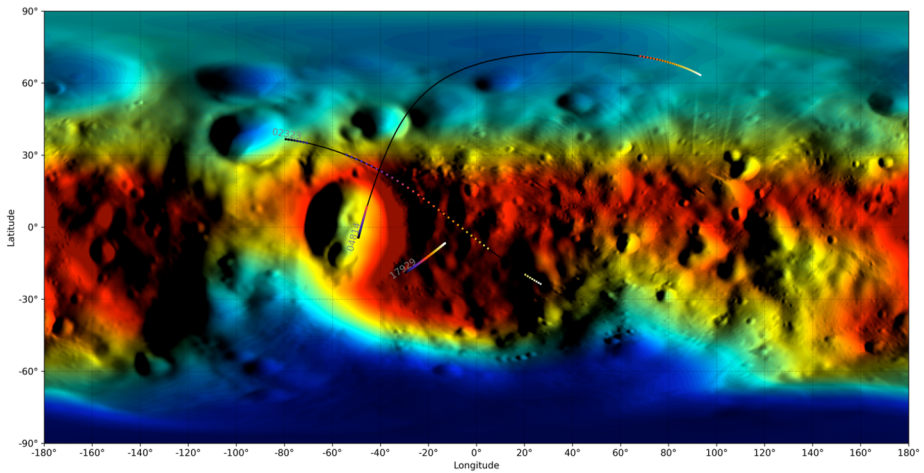


Fig. 7 Ground track projection of selected Phobos flybys

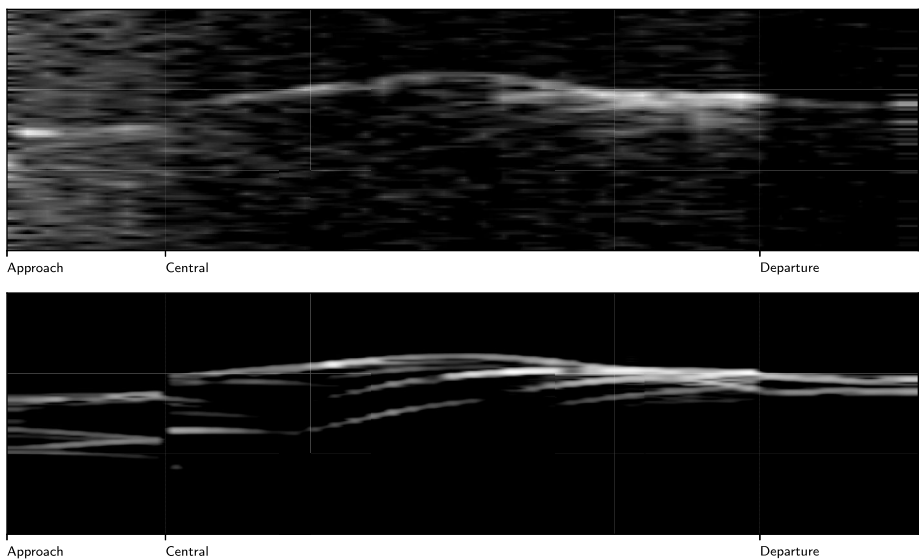


Fig. 8 Orbit 2323, November 4, 2005. Top: measured radar echoes, bottom: simulated surface backscattering. The approach segment (36.5 s) follows relatively flat terrain. The central segment (113.9 s) shows Phobos' irregular shape as well as the rims of the Stickney crater, which appear as delayed echoes. The departure segment (31.9 s) is above flat terrain, again. (Compare Fig. 7 for ground track projection)

The measurements revealed a number of secondary echoes that could have been caused by topographic relief or subsurface interfaces. To identify surface echoes, high-resolution shape models of Phobos (Gaskell 2002; Willner et al. 2010a, 2014) were employed in a radar backscattering simulator based on a physical-optics approach (Plettmeier et al. 2009). Running on a large-scale computer cluster, this simulator could produce accurate high-resolution results.

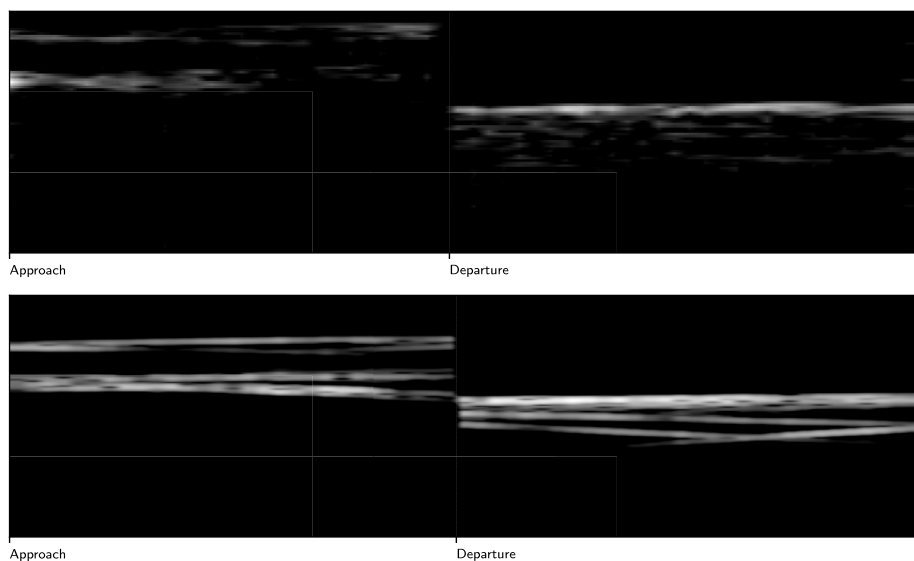


Fig. 9 Orbit 4814, October 10, 2007. Top: measured radar echoes, bottom: simulated surface backscattering. The approach segment crosses the Stickney Crater, showing echoes from the crater edges and the Limtoc Crater inside the Stickney Crater. The departure segment traverses the northern polar plateau, resulting in several echoes from craters located there. (Compare Fig. 7 for ground track projection)

Orbit 2323, as shown in Fig. 8, provided high-quality data in terms of SNR. However, due to limitations of the accessible onboard memory, this orbit had to be divided into three parts. The first and last parts corresponded to relatively flat terrain, while the middle part corresponded to steeply sloped terrain on the outer rim of Stickney crater (Fig. 7). Unfortunately, the comparison of simulations with real data did not reveal echoes that could be definitively identified as originating from the subsurface; all echoes visible in the MARSIS data could be reproduced by surface backscattering simulations. The brightness distribution for this orbit closely matched, especially in the crater region, but there was no conclusive evidence of subsurface interfaces. This could be due to the high slopes around Stickney inhibiting the formation of thick layering in the regolith.

In another early flyby, orbit 4814, high-quality data were obtained as the spacecraft crossed Stickney crater. As seen in Fig. 9, the later echoes were caused by different parts of the sloping terrain inside the Stickney crater, such as the Limtoc crater, while the first echoes corresponded to reflections from Stickney's rim. In the departure segment, where the terrain at high latitudes was relatively flat overall, the MARSIS measured data and the simulated data corresponded reasonably well [2].

The simulation results in Fig. 8 were based on a homogeneous permittivity distribution (with $\epsilon_r \approx 6$, based on laboratory measurements of analog material; Heggy et al. 2006). By comparing the brightness ratios of the different segments, differences between simulation and measurement could be discerned. This might be due to variations in reflectivity within the crater area. Notably, significant albedo differences in the optical range were observed by HiRise and HRSC cameras in the Stickney area (Thomas et al. 2011; Fraeman et al. 2014), which might also be present in the MARSIS radar frequencies. It's important to note that this variation doesn't necessarily indicate compositional differences; it may be caused by variations in porosity that affect the dielectric properties of the medium or sub-wavelength

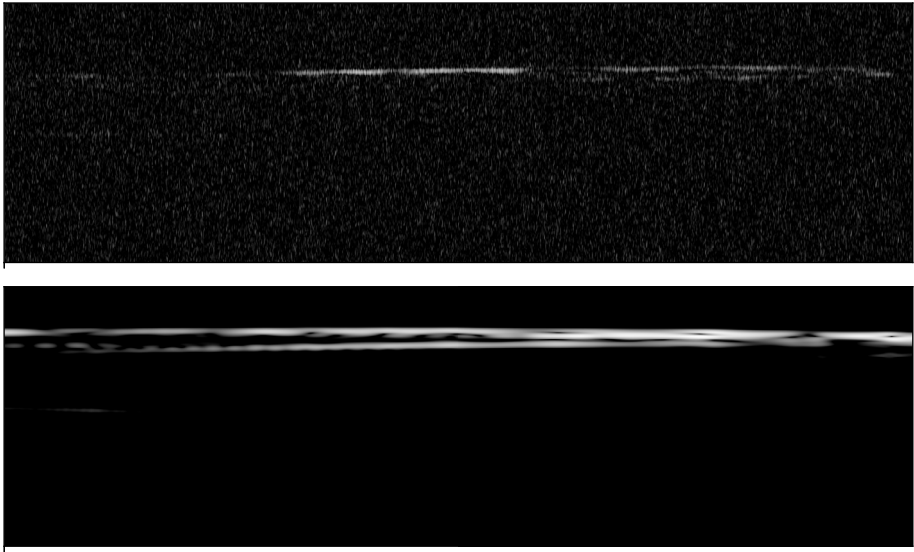


Fig. 10 Orbit 17929, March 2, 2018. Top: measured radar echoes, bottom: simulated surface backscattering. During the flyby, several smaller craters of Phobos' equatorial region are illuminated. All echoes in the measurement are present in the surface backscattering simulation. (Compare Fig. 7 for ground track projection)

scale surface roughness. However, the latter is unlikely because the MARSIS wavelength is so long that roughness would need to have an rms height variation of approximately 6 meters over an area extending many kilometers for signal attenuation to occur. The difference could also be attributed to different levels of subsurface fracturing induced by the impact bombardment of Phobos, or it may result from the crater bottom's concave shape, making later echoes brighter. Alternatively, it could be an indication of sedimentary fills in the crater floor.

In Fig. 10, the Phobos flyby during orbit 17929 is shown, traversing the elongated equatorial region of Phobos located to the East of the Stickney crater, north of the Kepler region – an area marked by grooves and smaller craters. In the initial segment, a delayed signal is evident in the measured data, also observable in the simulations, likely originating from the ridge of the Stickney crater. As observed in previous instances, all echoes can be attributed to surface features, and no definitive subsurface signatures have been identified. Additional flybys are presented and discussed in references Cicchetti et al. (2008, 2010, 2011, 2017) and Hegler et al. (2018), revealing similar overall findings.

Considering Phobos' notably low bulk density (Pätzold et al. 2014a), it is reasonable to hypothesize that the surface is covered with a relatively thin regolith or dust layer, on the order of a few meters, and that the internal structure is either fractured at a similar scale or porous. This would cause radar waves passing the surface to scatter and be absorbed, without returning to the receiver.

However, simulations indicated that certain echoes were weaker or stronger than expected for a uniform composition, likely due to variations in dielectric properties across the surface of Phobos affecting radar reflectivity. As a result, attempts were made to develop a method for solving the inverse problem of determining the distribution of surface dielectric properties on Phobos, through iterative matching between simulations and real data (Hegler

et al. 2011). The development of this method is ongoing, although some early results have already been presented.

Observations of Phobos remain challenging, and only a few of the flybys in which MAR-SIS operated produced high-quality data. Optimizing instrument parameters during flybys carries risks for the instrument and is performed with caution. Therefore, the lack of sub-surface interface detection does not rule out their existence or the potential for detection in future flybys. Large computational resources are required for simulations, and not all existing data have been thoroughly analyzed, necessitating continued planning and execution of Phobos observations (e.g. Cicchetti et al. 2011).

5.4 Space Environment

The Martian moons have also attracted space-plasma scientists because the moons can disturb the electromagnetic and plasma environments around Mars (Riedler et al. 1989; Dubinin et al. 1990; Barabash and Lundin 1994). Phobos and Deimos interact with both the solar wind and the Martian magnetotail plasma. The typical size of tens of km, which is in the range between the ion and electron gyro radii, makes the interaction with the solar wind unique. In addition, if gas or dust tori exist (Ip and Banaszekiewicz 1990), these would interact with the nearby plasma. Although there has been no evidence of the existence of tori, this interaction remains a point of interest (Fanale and Salvail 1989).

The physics of the interaction between Phobos and the solar wind is analogous to that of other non-magnetized celestial bodies, including Earth's moon, Ceres, the Galilean moons of Jupiter, and Mercury. This interaction is essentially a plasma-surface interaction, where the top layer of the regolith is exposed to the space environment. Notably, the regolith is recognized as an effective absorber of the upstream plasma. Consequently, it may record the history of solar wind protons, alpha particles, and Martian ionospheric oxygen (Ozima et al. 2008; Nénon et al. 2021).

However, this absorption is not perfect, as observed in the case of Earth's moon. Approximately 20% of the upstream plasma in the form of protons has been found to be backscattered (Saito et al. 2008; Wieser et al. 2009; McComas et al. 2009; Futaana et al. 2012; Lue et al. 2014). The charge state of the backscattered particles is mostly neutral, but a fraction of them (~ 0.1 – 1% of the incoming plasma) carries a positive charge. We expect the Phobos regolith surface to exhibit a similar backscattering of the upstream plasma.

With the ASPERA-3 experiment using the IMA instrument (Holmstrom et al., this journal), plasma measurements were conducted in June 2008 during a Mars Express flyby of Phobos, with the closest approach distance being less than 100 km. During this flyby, the IMA instrument recorded a peculiar signature of ions (Fig. 11) (Futaana et al. 2010).

While it was concluded that these ions were likely of Phobos origin through the backscattering process, other possibilities, such as foreshock ions, Martian ions, or ions originating from the spacecraft, could not be entirely ruled out. Subsequently, a second detection of protons during a flyby in 2016 was reported (Futaana et al. 2021).

The observed proton signatures were similar to those of the 2008 flyby in terms of energy range and sporadic features with a periodicity of around 3–5 minutes. It's noteworthy that MAVEN, during its Phobos flyby, did not detect any signals of ions (Deniau et al. 2022). This discrepancy is not necessarily contradictory to Mars Express observations since the Mars Express flybys have exhibited such signatures only twice out of more than 20 flybys at a sufficiently close distance. While the detection probability would be low, the reason behind the apparent difference compared to the Moon remains an open question.

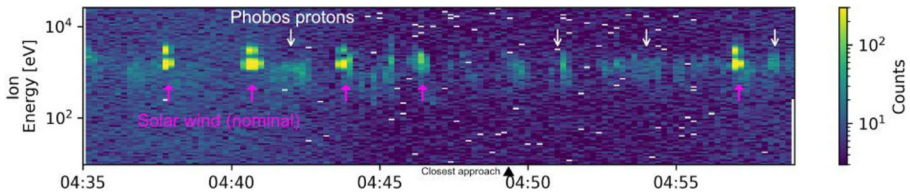


Fig. 11 The energy-time spectrogram measured by the IMA instrument during the Phobos flyby on July 23, 2008. The closest approach was approximately 74 km at 04:49. The high count signals (purple arrows) were nominal solar wind (the periodicity of around 3 minutes is due to the elevation scanning). The counts annotated by white arrows were not originating from the Sun's direction, and they were concluded to be protons backscattered from Phobos (Futaana et al. 2010)

In summary, the question of whether Phobos reflects solar wind protons is still a subject of debate. If the signal observed on Mars Express was not of Phobos origin, a more fundamental question arises: why does Phobos not backscatter solar wind protons as the Moon does? Several possibilities have been proposed (Futaana et al. 2021):

- The low probability of measuring backscattering from the small Phobos, considering its scale (approximately 10 km). The 6-dimensional phase space volume that reflected ions can occupy could be minuscule and highly variable.
- Electric or magnetic fields can interfere with solar wind precipitation on the Phobos surface. Hypothetical global magnetization (Mordovskaya et al. 2001) or small-scale geographical structures (Farrell et al. 2010) could potentially impede the backscattering process.
- Differences in Phobos regolith structures (grain size, composition, porosity, etc.) compared to those of the Moon could lead to variations in the backscattering process. There may also exist asymmetry between the near and far sides of Phobos (Nénon et al. 2021).

The potential measurements conducted by MMX/MSA (Yokota et al. 2021), in collaboration with Mars Express/IMA, are crucial. They aim to confirm the existence of backscattered protons from Phobos and to characterize the backscattering process (if it exists) or investigate the lack of such a process (if it does not exist). The debate surrounding backscattering processes on the Moon and Phobos may shed light on the diversity of their environments, regolith characteristics, and the physics of plasma-surface interaction. Valuable lessons from the Mars Express operations will be beneficial for MMX Phobos measurements. It is essential for the MMX and Mars Express teams to operate their instruments optimally by selecting the most suitable mode for Phobos. Special operations should be coordinated when Mars Express approaches Phobos. Conducting multiple measurements in proximity to Phobos will contribute to an enhanced understanding of Phobos' interaction with the solar wind and the Martian magnetotail.

6 Cartography and Mapping Data Products

Cartographic products serve as essential tools for scientists, enabling them to navigate and gain insights into unfamiliar terrains and previously unexplored regions. As a result, Phobos and Deimos have been systematically mapped and cartographically documented since the beginning of Mars exploration by orbital spacecraft with Mariner 9 (Turner 1978).

A comprehensive overview of the historical developments in the field of Martian moon cartography was provided by Wählisch et al. (2014). These cartographic products, like other

scientific data, have greatly benefited from information gathered by the scientific instruments aboard of MEX. Notably, higher-resolution image maps, derived from HRSC images (Wählisch et al. 2014), have resulted in cartographic products such as Geographic Information System (GIS) catalogs (Karachevtseva et al. 2012).

Orthorectified images, generated for Phobos mapping, have also played a crucial role in geological analysis, constraining the surface ages (Schmedemann et al. 2014). This, in turn, has contributed valuable insights into the origin of the Martian moons. The mapping efforts have further found application in various studies, including the modeling of the origin of the Phobos grooves, which has been explored through a variety of theories (Simioni et al. 2015; Murray and Heggie 2014; Ramsley and Head 2019).

In anticipation of the Phobos-Grunt mission, a combination of diverse datasets, such as geometric height, dynamic heights, and image data, was employed to characterize the prospective landing area of the lander (Willner et al. 2010b).

7 Putting It All Together

Mars Express has ushered in a new era of Phobos exploration with its elliptical orbit, allowing for regular flybys at unprecedented distances, including approaches as close as 50 km. Originally designed to observe Mars' surface and atmosphere, its instruments have produced a unique dataset that includes precise geophysical parameters, insights into Phobos' interior, high-resolution images, remote sensing data of its surface, and observations of the interactions between Phobos' surface and the space environment. This wealth of information has reignited scientific interest in a fundamental question about the Martian moons: how did they form?

The shape models enhanced the accuracy of the assumed forced libration amplitude, a critical factor in understanding Phobos' internal structure. This in turn sparked discussions on whether Phobos constitutes a rubble pile, a solid body, or a differentiated object, carrying significant implications for the two leading hypotheses concerning its origin: was it captured by Mars, or did it accrete in situ from a circum-Martian debris disk (Burns 1992; Andert et al. 2010; Rosenblatt 2011)?

Phobos' distinctive triaxial shape is more than mere happenstance, likely a result of its formation and evolutionary history. This leads toward the initial conclusion that Phobos is a rubble pile, a hypothesis that gains further credence when we consider its low bulk density of $(1860 \pm 13) \text{ kg/m}^3$ (Andert et al. 2010; Pätzold et al. 2014b; Willner et al. 2010a).

An important concept for tidally locked moons like Phobos is the equipotential surface that balances the gravitational, centrifugal, and Martian tidal potentials around the body (Soter and Harris 1977b). Using the shape model developed by Willner et al. (2010a) and the $G \cdot M$ value determined by the MEX-MaRS radio science experiment radio tracking (Andert et al. 2010; Pätzold et al. 2014b), Hu et al. (2020) calculated the best-fitting equipotential ellipsoid and formally measured the surface heights of Phobos, assuming a homogeneous mass distribution. Their findings revealed that Phobos' current shape significantly deviates from equilibrium in its current orbit at 2.76 Mars radii but would closely approach equilibrium at 3.3 Mars radii. This concept of equilibrium figures, possibly a signature of self-accretion under substantial tidal influence, is not a novel idea. Nevertheless, the precise details remain a subject of ongoing exploration (Soter and Harris 1977b). According to this scenario, Phobos likely formed from a debris disk just beyond the fluid Roche limit, at approximately 3.1 Mars radii. This distance is the critical threshold where hydrostatic equilibrium can be sustained. Given its progressively decreasing orbit, Phobos' accretion likely transpired around 80 million years ago.

Table 3 MEX instruments, their Phobos observation objectives and their conclusion on Phobos internal structure, composition and origin

Instrument	Objective	Conclusion on structure, composition and origin
ASPERA-3	space environment	
HRSC/SRC	positional measurements → ephemerides Shape model → volume, bulk density → best-fitting equipotential ellipsoid and surface heights Rotational model, in particular physical libration amplitude - cartography - surface morphology + crater statistics + grooves + landslides	rubble pile, accreted in situ formation from debris disk just beyond fluid Roche limit age dynamic orbital evolution
MaRS:	mass → bulk density, porosity → gravity field up to order 2	rubble pile, accreted in situ rubble pile, accreted in situ
MARSIS	subsurface	no conclusive evidence of subsurface interfaces
OMEGA	surface composition	captured D-type asteroid
PFS	surface composition	accreted in orbit
SPICAM	surface composition	no conclusion on origin

The rock material densities have implications on theory and speculations on the origin, the formation of Phobos (and Deimos) and on the evolution of their orbits under tidal forces (Rosenblatt 2011).

Andert et al. (2010) concluded that a porous Phobos may have accreted from a debris disk in Mars orbit and is therefore not a captured asteroid. It would explain the relative high porosity and the low bulk density. The origin of the debris disk is source of other speculations as Mars material blasted in Mars orbit by a giant impact on the Mars surface (Craddock 2011) or as material generated from an asteroid destroyed by gradient gravity forces when passing closely planet Mars (Rosenblatt 2011). If Phobos was re-accreted from material in Mars orbit, it makes Phobos a solar system object of at least second if not of higher generation (Hesselbrock Astron and Minton 2017).

This interpretation lends support to the results of a numerical investigation and the hypothesis presented by Hesselbrock Astron and Minton (2017). They suggest that Phobos has undergone multiple cycles of tidal disruption and re-accretion. The latter would have occurred as the debris ring, post-disruption, expanded beyond the Roche limit. This scenario offers an elegant resolution to the age dilemma, explaining why we are observing Phobos on the brink of imminent disruption in approximately 20-40 million years (Black and Mittal 2015). In contrast, a primordial body would have been several giga years old, nearing the end of its existence (Oberst et al. 2014). Consequently, Phobos may be seen as a recycled, remnant moon accreted in orbit, a second generation solar system object (Pätzold et al.

2012). A more comprehensive analysis will be possible with forthcoming refined gravity field solutions and shape models from the MMX mission (Kuramoto et al. 2022), promising deeper insights. This mission will be important for shedding light on the plausibility of this hypothesis.

Despite the wealth of data collected by Mars Express, remote sensing has not yet clearly identified the moon's surface composition (Fraeman et al. 2012; Giuranna et al. 2011; Ver-nazza et al. 2010; Pieters et al. 2014). This ambiguity prevents a definitive confirmation or refutation of the asteroid capture scenario, which likens Phobos to be a D-type asteroid (e.g., Pajola et al. 2013). Furthermore, the moons' current orbits contradict the capture scenario (Rosenblatt 2011) and present other unrealistic dynamical challenges (Cazenave et al. 1980).

Data from most instruments aboard Mars Express (Table 3) have supported the hypothesis that Phobos and Deimos formed through the accretion of a rocky debris disk in orbit around Mars (Craddock 2011; Rosenblatt and Charnoz 2012). The moons' refined shapes, low mass, and bulk density lend credence to this accretion scenario (Andert et al. 2010; Pätzold et al. 2014b; Hu et al. 2020). Additionally, the non-detection of MARSIS echoes suggests a porous interior, consistent with the low density and indicative of an accretion formation process in Mars' orbit (Pätzold et al. 2014b).

Further investigation of the Martian environment is needed to detect any remaining ring-forming material close to Mars, and to reveal the actual composition of Phobos and Deimos. This critical information could be obtained through the MMX mission, which will facilitate more precise observations at closer distances than those achievable with Mars Express fly-bys. Additionally, the mission aims to return a sample from Phobos to Earth for thorough compositional analysis (Usui et al. 2020).

Acknowledgements The MaRS and HRSC experiments were funded by the German Space Agency until 2021 and by a contract with NASA until 2020. The ASPERA-3 experiment is a joint effort between 15 laboratories in 10 countries sponsored by their national agencies as well as the various institutes and universities hosting their efforts. We especially acknowledge the Swedish National Space Agency for supporting the Principal Investigator institute, Swedish Institute of Space Physics. P.R. is financially supported by the Centre National D'Études Spatiales (CNES). Phobos & Deimos astrometric observations were supported by the Deutsche Forschungsgemeinschaft (DFG), research grant number OB 124/14-1. The efforts by the MEX Science Ground Segment at ESAC, in Spain, the Flight Dynamics and Flight Control Teams at ESOC, Germany, and the ground station crews at ESTRACK and in particular at the Deep Space Network for the Phobos close flybys are highly appreciated. The authors thank the HRSC Experiment team at DLR, Institute of Planetary Research, Berlin, and at Freie Universität Berlin, the HRSC Science Team, as well as the Mars Express Project teams at ESTEC, ESOC, and ESAC for their successful planning and acquisition of data as well as for making processed data available to the science teams.

Funding Information Open Access funding enabled and organized by Projekt DEAL.

Declarations

Competing Interests The authors have no competing interests to declare that are relevant to the content of this article.

Open Access This article is licensed under a Creative Commons Attribution 4.0 International License, which permits use, sharing, adaptation, distribution and reproduction in any medium or format, as long as you give appropriate credit to the original author(s) and the source, provide a link to the Creative Commons licence, and indicate if changes were made. The images or other third party material in this article are included in the article's Creative Commons licence, unless indicated otherwise in a credit line to the material. If material is not included in the article's Creative Commons licence and your intended use is not permitted by statutory regulation or exceeds the permitted use, you will need to obtain permission directly from the copyright holder. To view a copy of this licence, visit <http://creativecommons.org/licenses/by/4.0/>.

References

- Anderson JD (1971) Mariner Mars'69 celestial mechanics experiment. In: Sagan C, Owen TC, Smith HJ (eds) Planetary atmospheres, p 257
- Andert TP, Rosenblatt P, Pätzold M, et al (2010) Precise mass determination and the nature of Phobos. *Geophys Res Lett* 37(9):L09202. <https://doi.org/10.1029/2009GL041829>
- Archinal BA, Acton CH, A'Hearn MF, et al (2018) Report of the IAU working group on cartographic coordinates and rotational elements: 2015. *Celest Mech Dyn Astron* 130(3):22. <https://doi.org/10.1007/s10569-017-9805-5>
- Barabash S, Lundin R (1994) On a possible dust-plasma interaction at Mars. *IEEE Trans Plasma Sci* 22(2):173–178. <https://doi.org/10.1109/27.279020>
- Bertaux JL, Gondet B, Bibring JP, et al (2011) Combined albedo spectrum of Phobos in UV and visible with SPICAM and OMEGA on Mars Express. In: EPSC-DPS joint meeting 2011, p 523
- Black BA, Mittal T (2015) The demise of Phobos and development of a Martian ring system. *Nat Geosci* 8(12):913–917. <https://doi.org/10.1038/ngeo2583>
- Burmeister S, Willner K, Schmidt V, et al (2018) Determination of Phobos' rotational parameters by an inertial frame bundle block adjustment. *J Geod*: 1–11 <https://doi.org/10.1007/s00190-018-1112-8>
- Burns JA (1992) Contradictory clues as to the origin of the Martian moons. In: George M (ed) Mars. University of Arizona Press, Tucson, pp 1283–1301
- Cardesin-Moinelo A, Geiger B, Lacombe G, et al (2021) First year of coordinated science observations by Mars Express and ExoMars 2016 Trace Gas Orbiter. *Icarus* 353:113,707. <https://doi.org/10.1016/j.icarus.2020.113707>
- Cardesin-Moinelo A, Godfrey J, Grotheer E, et al (2024) Mars Express: 20 years of Mission, Science Operations and Archiving. *Space Sci Rev* 220(25). <https://doi.org/10.1007/s11214-024-01059-0>
- Cazenave A, Dobrovolskis A, Lago B (1980) Orbital history of the Martian satellites with inferences on their origin. *Icarus* 44(3):730–744. [https://doi.org/10.1016/0019-1035\(80\)90140-2](https://doi.org/10.1016/0019-1035(80)90140-2)
- Christensen EJ, Born GH, Hildebrand CE, et al (1977) The mass of Phobos from viking flybys. *Geophys Res Lett* 4(12):555–557. <https://doi.org/10.1029/GL004i012p00555>
- Cicchetti A, Calabrese D, Flamini E, et al (2008) Radar sounding of Phobos by MARSIS. In: AGU Fall Meeting abstracts, pp P42A–06
- Cicchetti A, Gim Y, Heggy E, et al (2010) MARSIS at Phobos: real data processing compared with simulations results. In: European Planetary Science Congress 2010, p 367
- Cicchetti A, Cartacci M, Gim Y, et al (2011) MARSIS: latest Phobos flyby. In: EPSC-DPS joint meeting 2011. Data processing results and advanced radar configuration design, p 497
- Cicchetti A, Nenna C, Plaut JJ, et al (2017) Observations of Phobos by the Mars Express radar MARSIS: description of the detection techniques and preliminary results. *Adv Space Res* 60(10):2289–2302. <https://doi.org/10.1016/j.asr.2017.08.013>
- Cicchetti A, Nenna C, Plaut J, et al (2023) Improvement of the MARSIS on-board SW, on the Mars Express mission. Preliminary scientific results on Phobos and Mars. In: XVIII congresso nazionale di scienze planetarie abstract book. <http://hdl.handle.net/20.500.12386/33973>
- Craddock RA (2011) Are Phobos and Deimos the result of a giant impact? *Icarus* 211(2):1150–1161. <https://doi.org/10.1016/j.icarus.2010.10.023>
- Deniau A, Nénon Q, André N, et al (2022) MAVEN proton observations near the Martian moon Phobos: does Phobos backscatter solar wind protons? *Geophys Res Lett* L101:014
- Desage L, Herique A, Lainey V, et al (2024) MARSIS data as a new constraint for the orbit of Phobos. *Astron Astrophys*. <https://doi.org/10.1051/0004-6361/202348655>
- Dubinin EM, Lundin R, Pissarenko NF, et al (1990) Indirect evidences for a gas/dust torus along the Phobos orbit. *Geophys Res Lett* 17(6):861–864. <https://doi.org/10.1029/GL017i006p00861>
- Duxbury TC (1974) Phobos: control network analysis. *Icarus* 23:290–299. [https://doi.org/10.1016/0019-1035\(74\)90007-4](https://doi.org/10.1016/0019-1035(74)90007-4)
- Duxbury TC (1991) An analytic model for the Phobos surface. *Planet Space Sci* 39:355–376. [https://doi.org/10.1016/0032-0633\(91\)90157-6](https://doi.org/10.1016/0032-0633(91)90157-6)
- Duxbury TC, Callahan JD (1989) PHOBOS and Deimos control networks. *Icarus* 77:275–286. [https://doi.org/10.1016/0019-1035\(89\)90090-0](https://doi.org/10.1016/0019-1035(89)90090-0)
- Fanale FP, Salvail JR (1989) Loss of water from Phobos. *Geophys Res Lett* 16(4):287–290. <https://doi.org/10.1029/GL016i004p00287>
- Farrell WM, Stubbs TJ, Halekas JS, et al (2010) Anticipated electrical environment within permanently shadowed lunar craters. *J Geophys Res* 115(E3)
- Fraeman AA, Arvidson RE, Murchie SL, et al (2012) Analysis of disk-resolved OMEGA and CRISM spectral observations of Phobos and Deimos. *J Geophys Res Planets* 117:E00J15. <https://doi.org/10.1029/2012JE004137>

- Fraeman AA, Murchie SL, Arvidson RE, et al (2014) Spectral absorptions on Phobos and Deimos in the visible/near infrared wavelengths and their compositional constraints. *Icarus* 229:196–205. <https://doi.org/10.1016/j.icarus.2013.11.021>
- Futaana Y, Barabash S, Holmström M, et al (2010) Backscattered solar wind protons by Phobos. *J Geophys Res* 115(A10)
- Futaana Y, Barabash S, Wieser M, et al (2012) Empirical Energy Spectra of Neutralized Solar Wind Protons from the Lunar Regolith. *J Geophys Res* 117(E5)
- Futaana Y, Holmström M, Fedorov A, et al (2021) Does Phobos reflect solar wind protons? Mars Express special flyby operations with and without the presence of Phobos. *J Geophys Res Planets* E006:969
- Gaskell RW (2002) Three dimensional landmark templates. In: AGU Fall Meeting abstracts, pp P21A–0359
- Giese B, Oberst J, Scholten F, et al (2005) Ein hoch auflösendes Oberflächenmodell des Marsmondes Phobos. In: *Photogrammetrie Fernerkundung Geoinformation*, pp 439–444. LIDO-Berichtsjahr
- Giuranna M, Roush TL, Duxbury T, et al (2011) Compositional interpretation of PFS/MEx and TES/MGS thermal infrared spectra of Phobos. *Planet Space Sci* 59(13):1308–1325. <https://doi.org/10.1016/j.pss.2011.01.019>
- Gwinner K, Jaumann R, Hauber E, et al (2016) The High Resolution Stereo Camera (HRSC) of Mars Express and its approach to science analysis and mapping for Mars and its satellites. *Planet Space Sci* 126:93–138. <https://doi.org/10.1016/j.pss.2016.02.014>
- Hall A (1877) Observations of the satellites of Mars. *Astron Nachr* 91(1):11. <https://doi.org/10.1002/asna.18780910103>
- Heggy E, Clifford SM, Grimm RE, et al (2006) Ground-penetrating radar sounding in mafic lava flows: assessing attenuation and scattering losses in Mars-analog volcanic terrains. *J Geophys Res Planets* 111(E6):E06S04. <https://doi.org/10.1029/2005JE002589>
- Hegler S, Statz C, Plettemeier D, et al (2011) Surface epsilon_r reconstruction of Phobos. In: EPSC-DPS joint meeting 2011, p 1349
- Hegler S, Plettemeier D, Chicchetti A, et al (2018) MARSIS observations of Phobos: preliminary results of the search for underground reflectors. In: *European Planetary Science Congress*, pp EPSC2018–1044
- Hernandez-Bernal J, Cardesín-Moinelo A, Hueso R, et al (2024) The Visual Monitoring Camera (VMC) on Mars Express: A new science instrument made from an old webcam orbiting Mars. *Planet Space Sci* 251:105972. <https://doi.org/10.1016/j.pss.2024.105972>
- Hesselbrock Astron J, Minton DA (2017) An ongoing satellite-ring cycle of Mars and the origins of Phobos and Deimos. *Nat Geosci* 10(4):266–269. <https://doi.org/10.1038/ngeo2916>
- Housen KR, Holsapple KA, Voss ME (1999) Compaction as the origin of the unusual craters on the asteroid Mathilde. *Nature* 402(6758):155–157. <https://doi.org/10.1038/45985>
- Hu X, Oberst J, Willner K (2020) Equipotential figure of Phobos suggests its late accretion near 3.3 Mars radii. *Geophys Res Lett* 47(7):e85958. <https://doi.org/10.1029/2019GL085958>
- Ip WH, Banaszkiwicz M (1990) On the dust/gas tori of Phobos and Deimos. *Geophys Res Lett* 17(6):857–860. <https://doi.org/10.1029/GL017i006p00857>
- Jacobson RA (2010) The orbits and masses of the Martian satellites and the libration of Phobos. *Astron J* 139(2):668–679. <https://doi.org/10.1088/0004-6256/139/2/668>
- Jacobson RA, Lainey V (2014) Martian satellite orbits and ephemerides. *Planet Space Sci* 102:35–44. <https://doi.org/10.1016/j.pss.2013.06.003>
- Jacobson RA, Konopliv AS, Park RS, et al (2018) The rotational elements of Mars and its satellites. *Planet Space Sci* 152:107–115. <https://doi.org/10.1016/j.pss.2017.12.020>
- Jaumann R, Neukum G, Behnke T, et al (2007) The high-resolution stereo camera (HRSC) experiment on Mars Express: instrument aspects and experiment conduct from interplanetary cruise through the nominal mission. *Planet Space Sci* 55(7–8):928–952. <https://doi.org/10.1016/j.pss.2006.12.003>
- Karachvtseva I, Oberst J, Shingareva K, et al (2012) Global Phobos geodatabase and GIS analyses. In: 43rd Annual Lunar and Planetary Science Conference, Lunar and Planetary Institute, p 1342
- Kolyuka YF, Ephimov AE, Kudryavtsev SM, et al (1990) Improved determination of the gravitational constant of Phobos on the basis of Phobos-2 trajectory tracking. *Pisma v Astron Zh* 16:396–400
- Kuramoto K, Kawakatsu Y, Fujimoto M, et al (2022) Martian Moons Exploration MMX: sample return mission to Phobos elucidating formation processes of habitable planets. *Earth Planets Space* 74(1):12. <https://doi.org/10.1186/s40623-021-01545-7>
- Lainey V, Dehant V, Pätzold M (2007) First numerical ephemerides of the Martian moons. *Astron Astrophys* 465(3):1075–1084. <https://doi.org/10.1051/0004-6361/20065466>
- Lainey V, Pasewaldt A, Robert V, et al (2021) Mars moon ephemerides after 14 years of Mars Express data. *Astron Astrophys* 650:A64. <https://doi.org/10.1051/0004-6361/202039406>. [arXiv:2009.06482](https://arxiv.org/abs/2009.06482) [astro-ph.EP]
- Lue C, Futaana Y, Barabash S, et al (2014) Chandrayaan-1 observations of backscattered solar wind protons from the lunar regolith: dependence on the solar wind speed. *J Geophys Res* 119:968–975

- McComas DJ, Allegrini F, Bochsler P, et al (2009) Lunar backscatter and neutralization of the solar wind: First observations of neutral atoms from the Moon. *Geophys Res Lett* 36(12)
- Mordovskaya VG, Oraevsky VN, Styashkin VA, et al (2001) Experimental evidence of the Phobos magnetic field. *JETP Lett* 74(6):293–297
- Murray JB, Heggie DC (2014) Character and origin of Phobos' grooves. *Planet Space Sci* 102:119–143. <https://doi.org/10.1016/j.pss.2014.03.001>
- Nénon Q, Poppe AR, Rahmati A, et al (2021) Implantation of Martian atmospheric ions within the regolith of Phobos. *Nat Geosci* 14(2):61–66. <https://doi.org/10.1038/s41561-020-00682-0>
- Oberst J, Hoffmann H, Matz KD, et al (2006a) New observations of Phobos and its shadow with the HRSC/SRC on Mars Express. In: Mackwell S, Stansbery E (eds) 37th Annual Lunar and Planetary Science Conference, Lunar and Planetary Institute, p 1312
- Oberst J, Matz KD, Roatsch T, et al (2006b) Astrometric observations of Phobos and Deimos with the SRC on Mars Express. *Astron Astrophys* 447(3):1145–1151. <https://doi.org/10.1051/0004-6361/20053929>
- Oberst J, Schwarz G, Behnke G, Behnke T, et al (2008) The imaging performance of the SRC on Mars Express. *Planet Space Sci* 56(3–4):473–491. <https://doi.org/10.1016/j.pss.2007.09.009>
- Oberst J, Zubarev A, Nadezhdina I, et al (2014) The Phobos geodetic control point network and rotation model. *Planet Space Sci* 102:45–50. <https://doi.org/10.1016/j.pss.2014.03.006>
- Ozima M, Yin QZ, Podosek F, et al (2008) Toward understanding early Earth evolution: prescription for approach from terrestrial noble gases and light elements records in lunar soils. *Geochim Cosmochim Acta, Suppl* 72(12):A714
- Pajola M, Lazzarin M, Dalle Ore CM, et al (2013) Phobos as a D-type captured asteroid, spectral modeling from 0.25 to 4.0 μm . *Astrophys J* 777(2):127. <https://doi.org/10.1088/0004-637X/777/2/127>
- Pasewaldt A, Oberst J, Willner K, et al (2012) New astrometric observations of Deimos with the SRC on Mars Express. *Astron Astrophys* 545:A144. <https://doi.org/10.1051/0004-6361/201118603>
- Pasewaldt A, Oberst J, Willner K, et al (2015) Astrometric observations of Phobos with the SRC on Mars Express. New data and comparison of different measurement techniques. *Astron Astrophys* 580:A28. <https://doi.org/10.1051/0004-6361/201525957>
- Pätzold M, Wennmacher A, Häusler B, et al (2001) Mass and density determinations of 140 Siwa and 4979 Otawara as expected from the Rosetta flybys. *Astron Astrophys* 370:1122–1127. <https://doi.org/10.1051/0004-6361:20010244>
- Pätzold M, Andert TP, Asmar SW, et al (2011) Asteroid 21 Lutetia: low mass, high density. *Science* 334(6055):491. <https://doi.org/10.1126/science.1209389>
- Pätzold M, Andert T, Häusler B, et al (2012) Ashes to Ashes, Dust to Dust: Phobos, the Life and Fate of an Inhomogeneous Moon of Second Generation. In: AAS/Division for Planetary Sciences Meeting Abstracts, #44, p 211.01
- Pätzold M, Andert T, Jacobson R, et al (2014a) Phobos: observed bulk properties. *Planet Space Sci* 102:86–94. <https://doi.org/10.1016/j.pss.2014.01.004>
- Pätzold M, Andert TP, Tyler GL, et al (2014b) Phobos mass determination from the very close flyby of Mars Express in 2010. *Icarus* 229:92–98. <https://doi.org/10.1016/j.icarus.2013.10.021>
- Picardi G, Plaut JJ, Biccari D, et al (2005) Radar soundings of the subsurface of Mars. *Science* 310(5756):1925–1928. <https://doi.org/10.1126/science.1122165>
- Pieters CM, Murchie S, Thomas N, et al (2014) Composition of surface materials on the moons of Mars. *Planet Space Sci* 102:144–151. <https://doi.org/10.1016/j.pss.2014.02.008>
- Plettmeier D, Hahnel R, Hegler S, et al (2009) Simulation of radar-backscattering from Phobos - a contribution to the experiment MARSIS aboard MarsExpress. In: EGU General Assembly Conference Abstracts, EGU / Copernicus, p 3763
- Pollack JB, Veverka J, Noland M, et al (1972) Mariner 9 television observations of Phobos and Deimos. *Icarus* 17(2):394–407. [https://doi.org/10.1016/0019-1035\(72\)90007-3](https://doi.org/10.1016/0019-1035(72)90007-3)
- Rambaux N, Castillo-Rogez JC, Le Maistre S, et al (2012) Rotational motion of Phobos. *Astron Astrophys* 548:A14. <https://doi.org/10.1051/0004-6361/201219710>
- Ramsley KR, Head JW (2017) The Stickney Crater ejecta secondary impact crater spike on Phobos: implications for the age of Stickney and the surface of Phobos. *Planet Space Sci* 138(Supplement C):7–24. <https://doi.org/10.1016/j.pss.2017.02.004>
- Ramsley KR, Head JW (2019) Origin of Phobos grooves: testing the Stickney Crater ejecta model. *Planet Space Sci* 165:137–147. <https://doi.org/10.1016/j.pss.2018.11.004>
- Riedler W, Möhlmann D, Oraevsky VN, et al (1989) Magnetic fields near Mars: first results. *Nature* 341(6243):604–607. <https://doi.org/10.1038/341604a0>
- Rosenblatt P (2011) The origin of the Martian moons revisited. *Astron Astrophys Rev* 19:44. <https://doi.org/10.1007/s00159-011-0044-6>
- Rosenblatt P, Charnoz S (2012) On the formation of the Martian moons from a circum-Martian accretion disk. *Icarus* 221(2):806–815. <https://doi.org/10.1016/j.icarus.2012.09.009>

- Rosenblatt P, Lainey V, Le Maistre S, et al (2008) Accurate Mars Express orbits to improve the determination of the mass and ephemeris of the Martian moons. *Planet Space Sci* 56:7. <https://doi.org/10.1016/j.pss.2008.02.004>
- Rosenblatt P, Charnoz S, Dunseath KM, et al (2016) Accretion of Phobos and Deimos in an extended debris disc stirred by transient moons. *Nat Geosci* 9(8):581–583. <https://doi.org/10.1038/ngeo2742>
- Safaieili A, Cicchetti A, Nenna C, et al (2007) Radar Sounder Observation of Phobos. In: First International Conference on the Exploration of Phobos and Deimos. Lunar and Planetary Institute, p 34
- Saito Y, Yokota S, Tanaka T, et al (2008) Solar wind proton reflection at the lunar surface: Low energy ion measurement by MAP-PACE onboard SELENE (KAGUYA). *Geophys Res Lett* 35:L24205. <https://doi.org/10.1029/2008GL036077>
- Samuel H, Lognonné P, Panning M, et al (2019) The rheology and thermal history of Mars revealed by the orbital evolution of Phobos. *Nature* 569(7757):523–527. <https://doi.org/10.1038/s41586-019-1202-7>
- Schmedemann N, Michael GG, Ivanov BA, et al (2014) The age of Phobos and its largest crater. *Stickney Planet Space Sci* 102:152–163. <https://doi.org/10.1016/j.pss.2014.04.009>
- Sharpless BP (1945) Secular accelerations in the longitudes of the satellites of Mars. *Astron J* 51:185–186. <https://doi.org/10.1086/105871>
- Shi X, Willner K, Oberst J, et al (2012) Working models for the gravitational field of Phobos. *Sci China, Phys Mech Astron* 55:358–364. <https://doi.org/10.1007/s11433-011-4606-4>
- Shi X, Oberst J, Willner K (2016) Mass wasting on Phobos triggered by an evolving tidal environment. *Geophys Res Lett* 43(24):12,371–12,379. <https://doi.org/10.1002/2016GL071650>
- Simioni E, Pajola M, Massironi M, et al (2015) Phobos grooves and impact craters: a stereographic analysis. *Icarus* 256:90–100. <https://doi.org/10.1016/j.icarus.2015.04.009>
- Soter S, Harris A (1977a) Are striations on Phobos evidence for tidal stress. *Nature* 268:421. <https://doi.org/10.1038/268421a0>
- Soter S, Harris A (1977b) The equilibrium figures of Phobos and other small bodies. *Icarus* 30(1):192–199. [https://doi.org/10.1016/0019-1035\(77\)90133-6](https://doi.org/10.1016/0019-1035(77)90133-6)
- Stark A, Willner K, Burmeister S, et al (2017) Geodetic framework for Martian satellite exploration I: reference rotation models. In: European Planetary Science Congress, pp EPSC2017–868
- Thomas P, Veverka J, Duxbury TC (1978) Origin of the grooves on Phobos. *Nature* 273:282–284. <https://doi.org/10.1038/273282a0>
- Thomas PC, Yoder CF, Synnott SP, et al (2000) Small Body Shape Models V2.1. NASA Planetary Data System EAR-A-5-DDR-SHAPE-MODELS-V2.1
- Thomas N, Stelter R, Ivanov A, et al (2011) Spectral heterogeneity on Phobos and Deimos: HiRISE observations and comparisons to Mars Pathfinder results. *Planet Space Sci* 59(13):1281–1292. <https://doi.org/10.1016/j.pss.2010.04.018>
- Tolson RH, Blackshear WT, Mason ML, et al (1977) The mass of Phobos. *Geophys Res Lett* 4(12):551–554. <https://doi.org/10.1029/GL004012p00551>
- Turner RJ (1978) A model of Phobos. *Icarus* 33(1):116–140. [https://doi.org/10.1016/0019-1035\(78\)90028-3](https://doi.org/10.1016/0019-1035(78)90028-3)
- Usui T, Bajo K, Fujjya W, et al (2020) The importance of Phobos sample return for understanding the Mars-Moon system. *Space Sci Rev* 216(4):49. <https://doi.org/10.1007/s11214-020-00668-9>
- Vernazza P, Cipriani F, Dukes C, et al (2010) Origin of the Martian moons: investigating their surface composition. In: European Planetary Science Congress 2010, p 262
- Wählisch M, Stooke P, Karachevtseva I, et al (2014) Phobos and Deimos cartography. *Planet Space Sci* 102:60–73. <https://doi.org/10.1016/j.pss.2013.05.012>
- Weiss BP, Elkins-Tanton LT, Antonietta Barucci M, et al (2012) Possible evidence for partial differentiation of asteroid Lutetia from Rosetta. *Planet Space Sci* 66(1):137–146. <https://doi.org/10.1016/j.pss.2011.09.012>
- Wieser M, Barabash S, Futaana Y, et al (2009) Extremely high reflection of solar wind protons as neutral hydrogen atoms from regolith in space. *Planet Space Sci* 57:2132–2134
- Williams BG, Duxbury TC, Hildebrand CE (1988) Improved determination of Phobos and Deimos masses from Viking fly-bys. In: Lunar and Planetary Science Conference, p 1274
- Willner K, Oberst J, Wählisch M, et al (2008) New astrometric observations of Phobos with the SRC on Mars Express. *Astron Astrophys* 488(1):361–364. <https://doi.org/10.1051/0004-6361/200809787>
- Willner K, Oberst J, Hussmann H, et al (2010a) Phobos control point network, rotation, and shape. *Earth Planet Sci Lett* 294(3–4):541–546. <https://doi.org/10.1016/j.epsl.2009.07.033>
- Willner K, Oberst J, Scholten F, et al (2010b) Phobos DTM and coordinate refinement for Phobos-Grunt mission support. In: European Planetary Science Congress 2010, p 222
- Willner K, Shi X, Oberst J (2014) Phobos' shape and topography models. *Planet Space Sci* 102:51–59. <https://doi.org/10.1016/j.pss.2013.12.006>
- Witasse O, Duxbury T, Chicarro A, et al (2014) Mars Express investigations of Phobos and Deimos. *Planet Space Sci* 102:18–34. <https://doi.org/10.1016/j.pss.2013.08.002>

- Yang X, Yan JG, Andert T, et al (2019) The second-degree gravity coefficients of Phobos from two Mars Express flybys. *Mon Not R Astron Soc* 490:2007–2012. <https://doi.org/10.1093/mnras/stz2695>
- Yokota S, Terada N, Matsuoka A, et al (2021) In situ observations of ions and magnetic field around Phobos: the mass spectrum analyzer (MSA) for the Martian Moons Exploration (MMX) mission. *Earth Planets Space* 73(1):216
- Ziese R, Willner K (2018) Mutual event observations of Solar System objects by SRC on Mars Express. Analysis and release of observations. *Astron Astrophys* 614:A15. <https://doi.org/10.1051/0004-6361/201731644>

Publisher's Note Springer Nature remains neutral with regard to jurisdictional claims in published maps and institutional affiliations.

Authors and Affiliations

Martin Pätzold¹  · Tom P. Andert² · Alejandro Cardesín-Moinelo³ · Andrea Cicchetti⁴ · Thomas Duxbury⁵ · Yoshifumi Futaana⁶ · James Godfrey⁷ · Sebastian Hegler⁸ · Xuanyu Hu⁹ · Valéry Lainey¹⁰ · Klaus-Dieter Matz¹¹ · Jürgen Oberst⁹ · Roberto Orosei¹² · Dirk Plettemeier⁸ · Pascal Rosenblatt¹³ · Alexander Stark¹¹ · Konrad Willner¹¹ · Olivier Witasse¹⁴ · Ramona Ziese^{9,11}

✉ M. Pätzold
Martin.Paetzold@uni-koeln.de

T.P. Andert
Tom.Andert@unibw.de

A. Cardesín-Moinelo
alejandro.cardesin@ext.esa.int

A. Cicchetti
andrea.cicchetti@inaf.it

T. Duxbury
tduxbury@gmu.edu

Y. Futaana
futaana@irf.se

J. Godfrey
james.godfrey@esa.int

S. Hegler
sebastian.hegler@tu-dresden.de

X. Hu
xuanyuhu@gmail.com

V. Lainey
valery.lainey@obspm.fr

K.-D. Matz
klaus-dieter.matz@dlr.de

J. Oberst
juergen.oberst@tu-berlin.de

R. Orosei
roberto.oroisei@inaf.it

D. Plettemeier
dirk.plettemeier@tu-dresden.de

P. Rosenblatt
pascal.rosenblatt@univ-nantes.fr

A. Stark
alexander.stark@dlr.de

K. Willner
konrad.willner@dlr.de

O. Witasse
olivier.witasse@esa.int

R. Ziese
ziese@tu-berlin.de

- 1 Abt. Planetenforschung, Rheinisches Institut für Umweltforschung an der Universität zu Köln, Cologne, Germany
- 2 Institut für Raumfahrttechnik und Weltraumforschung, Universität der Bundeswehr München, Neubiberg, Germany
- 3 European Space Astronomy Centre, ESA-ESAC, Madrid, Spain
- 4 Istituto di Astrofisica e Planetologia Spaziali, Istituto Nazionale di Astrofisica, Rome, Italy
- 5 George Mason University, Fairfax, VA, USA
- 6 Swedish Institute of Space Physics, Kiruna, Sweden
- 7 European Space Operations Centre, ESA-ESOC, Darmstadt, Germany
- 8 Professur Nachrichtentechnik, Technische Universität Dresden, Dresden, Germany
- 9 Institut für Geodäsie und Geoinformationstechnik, Planetengeodäsie, Technische Universität Berlin, Berlin, Germany
- 10 IMCCE, Observatoire de Paris, PSL Research University, CNRS, Sorbonne Université, Univ. Lille, Paris, France
- 11 Institut für Planetenforschung, DLR, Berlin-Adlershof, Germany
- 12 Istituto di Radioastronomia, Istituto Nazionale di Astrofisica, Bologna, Italy
- 13 Laboratoire de Planétologie et Géosciences, UMR6112, CNRS, Nantes Université, Université d'Angers, Le Mans Université, Nantes, France
- 14 European Space Research and Technology Centre, ESA-ESTEC, Noordwijk, The Netherlands